Professor Grasemann
Handling Topical Editor, Solid Earth

March 18th 2017

Dear Professor Grasemann

We thank you for reviewing our manuscript and are grateful for your editorial advice that coordinates should be added to our field locations. Coordinates have now been added to Table S2 for all field measuring stations. The localities depicted in Figure 2, 8a, and 8g were not used as field measuring stations, and so their coordinates are given in the figure captions themselves.

In addition, we have made minor revisions to the text to correct typos or where the wording could have been clarified. We thank you for your consideration of our manuscript and we look forward to hearing from you in the near future.

Yours sincerely

Dr Jack Williams

Dr Jack Williams
Research Associate in Structural Geology
School of Earth and Ocean Sciences
Cardiff University
Main Building
Cardiff
CF10 3AT
Phone: +44 (0)29 2087 4336
Email: JWilliams132@cardiff.ac.uk

Dr Jack Williams
Cysylltiad Ymchwil mewn Daeareg Strwythurol
Ysgol Gwyddorau'r Ddaear a'r Mor
Prifysgol Caerdydd
Prif Adeilad
Caerdydd
CF10 3AT
Ffôn : +44 (0)29 2087 4336
Ebost: JWilliams132@cardiff.ac.uk

26 **Controls on fault zone structure and brittle fracturing in the foliated hanging-**

27 **wall of the Alpine Fault**

29 Jack N. Williams[a]*, Virginia G. Toy[a], Cécile Massiot[b,c], David D. McNamara[c,d], Steven A. F.

30 Smith[a], Steven Mills[e]

31 **Affiliations:**

32 [a]Department of Geology, University of Otago, PO Box 56, Dunedin 9054, New Zealand

33 [b]School of Geography, Environment, and Earth Sciences, Victoria University of Wellington,

34 PO Box 600, Wellington 6012, New Zealand

35 [c]GNS Science, PO Box 30-368, Lower Hutt 5040, New Zealand

36 [d]Department of Earth and Ocean Sciences, NUI Galway, University Road, Galway, Ireland

37 [e]Department of Computer Science, University of Otago, PO Box 56, Dunedin 9054, New

38 Zealand

39 [*]**Corresponding Author:** Jack Williams, now at: School of Earth and Ocean Sciences,

40 Cardiff University, Cardiff, CF10 3AT, United Kingdom (email: williamsj132@cardiff.ac.uk)

42 **Abstract**

43 Three datasets are used to quantify fracture density, orientation, and fill in the foliated

44 hanging-wall of the Alpine Fault: (1) X-ray computed tomography (CT) images of drill-core

45 collected within 25 m of its principal slip zones (PSZs) during the first phase of the Deep

46 Fault Drilling Project that were reoriented with respect to borehole televiewer images, (2)

47 field measurements from creek sections up to 500 m from the PSZs, and (3) CT images of

48 oriented drill-core collected during the Amethyst Hydro Project at distances of ~0.7-2 km

49 from the PSZs. Results show that within 160 m of the PSZs in foliated cataclasites and

50 ultramylonites, gouge-filled fractures exhibit a wide range of orientations. At these distances,

51 fractures are interpreted to have formed at relatively high confining pressures and/or in rocks

52 that had a weak mechanical anisotropy. Conversely, at distances greater than 160 m from the

53 PSZs, fractures are typically open and subparallel to the mylonitic or schistose foliation,

54 implying that fracturing occurred at low confining pressures and/or in rocks that were

55 mechanically anisotropic. Fracture density is similar across the ~500 m width of the field

56 transects. By combining our datasets with measurements of permeability and seismic velocity

57 around the Alpine Fault, we further develop the hierarchical model for hanging-wall damage

58 structure that was proposed by Townend et al., (2017). The wider zone of foliation-parallel

59 fractures represents an 'outer damage zone' that forms in the near-surface. The distinct <160

60 m wide interval of widely oriented gouge-filled fractures constitutes an 'inner damage zone.'

61 This zone is interpreted to extend towards the base of the seismogenic crust given that its

62 width is comparable to: (1) the Alpine Fault low-velocity zone detected by fault zone guided

63 waves, and (2) damage zones reported from other exhumed large-displacement faults. In

64 summary, a narrow zone of fracturing at the base of the Alpine Fault's hanging-wall

65 seismogenic crust is anticipated to widen in the near-surface, which is consistent with fault

66 zone flower structure models.

67 **Keywords**: fractures, anisotropy, Alpine Fault, Deep Fault Drilling Project, damage zone

68 **1. Introduction**

69 Conceptual models of fault zone structure in the upper crust often invoke a relatively narrow

70 "fault core" that accommodates most displacement, surrounded by a halo of heavily fractured

71 rock termed the "damage zone" (Caine et al., 1996; Chester et al., 1993; Chester and Logan,

72 1986; Faulkner et al., 2010). These models have been successfully applied in a variety of

73 tectonic settings and for a wide range of fault displacements and exhumation depths (e.g.

74 Choi et al., 2016; Faulkner et al., 2010; Kim et al., 2004; Mitchell and Faulkner, 2009;

75 Savage and Brodsky, 2011). However, the term "damage zone" has been applied by

geologists and geophysicists to describe a variety of fault-related features, such as fractures and faults at stepovers and bends (Chester and Chester, 2000; Kim et al., 2004; Mitchell and Faulkner, 2009; Wilson et al., 2003), the volume of inelastic deformation that is induced by dynamic stresses during earthquake rupture propagation (Andrews, 2005; Cowie and Scholz, 1992; Rice et al., 2005; Templeton et al., 2008; Vermilye and Scholz, 1998), and the volume of rock in which earthquake swarms or foreshock and aftershock sequences are localised (Kim and Sanderson, 2008; Savage et al., 2017; Sibson, 1989; Yukutake et al., 2011). Furthermore, though damage zones are typically reported to be <1 km wide (Faulkner et al., 2011; Savage and Brodsky, 2011), co-seismic ground shaking can modify fracture permeability many hundreds of kilometres away from the fault source (Cox et al., 2015; Muir-Wood and King, 1993; O'Brien et al., 2016).

Brittle faults often develop in mylonite sequences or other (e.g. jointed) rocks that contain compositional and mechanical anisotropies (Bistacchi et al., 2012; Chester and Fletcher, 1997; Massironi et al., 2011). Evidence from field studies (Bistacchi et al., 2010; Peacock and Sanderson, 1992), experiments (Donath, 1961; Misra et al., 2015; Paterson and Wong, 2005), and numerical modelling (Chester and Fletcher, 1997) demonstrates that such anisotropy can significantly affect the orientation and density of brittle fractures. Despite this, "fault core-damage zone" models are based largely on field observations from relatively isotropic host rocks, and there have been comparatively few field studies (a notable exception being, Bistacchi et al., (2010)) that document the influence of mechanical anisotropy on patterns of brittle fracture damage in large-displacement faults.

In this contribution, multiple datasets across a range of scales were used to analyse fracture densities, orientations, and mineral fills across the hanging-wall of the Alpine Fault's central section. Measurements from within 25 m of the Alpine Fault principal slip zones (PSZs) were made from shallow (depths <130 m) drill-cores and wireline logs obtained during the first

103 phase of the Deep Fault Drilling Project (DFDP-1). These are combined with field studies at

104 distances <500 m from the PSZs and analyses of drill-core recovered at 0.7-2 km from the

105 PSZs during the Amethyst Hydro Project (AHP). Results are then compared to measurements

106 of hydraulic conductivity (Cox et al., 2015; Townend et al., 2017) and geophysical studies

107 (Boese et al., 2012; Chamberlain et al., 2017; Eccles et al., 2015) around the Alpine Fault. In

108 doing so, we critically assess the application of "damage zone" models to an active plate-

109 boundary-scale structure. Furthermore, the Alpine Fault rapidly exhumes ductile-to-brittle

110 fault rock sequences from depths of up to 35 km (Little et al., 2005; Norris and Toy, 2014).

111 Fracturing in its hanging-wall therefore overprints a 1-2 km wide mylonite sequence

112 containing a pervasive foliation (Cooper and Norris, 1994; Norris and Cooper, 1997, 2007;

113 Toy, 2008), and so can provide new insights into the relationships between fracturing and

114 mechanical anisotropy.

115

2. Tectonic setting of the Alpine Fault

117 The Alpine Fault is a crustal-scale (along strike extent ~850 km, depth ~35 km) transpressive

118 discontinuity accommodating ~70% of Pacific-Australian plate motion in the South Island of

119 New Zealand (DeMets et al., 1994; Norris and Cooper, 2001, Figure 1a). This study focuses

120 on the central section between the Toharoa and Martyr Rivers (Barth et al., 2013) where it

121 currently accommodates dextral strike-slip at a rate of 27 ± 5 mm/yr and dip-slip at a rate of

122 6-10 mm/yr (Little et al., 2005; Norris and Cooper, 2001).

123

124 In the central section at depths greater than 8-12 km, the Alpine Fault accommodates motion

125 via viscous creep across a >1 km wide ductile shear zone in which the hanging-wall "Alpine

126 Schist" protolith is progressively mylonitised (Norris and Cooper, 2007; Toy et al., 2010).

127 Shear strains increase with proximity to the Alpine Fault and are recorded by protomylonites,

129 mylonites and ultramylonites, which occur in spatial sequence towards the fault (Figure 2;

130 Norris and Cooper, 2003; Reed, 1964; Toy et al., 2008). Foliation in the mylonite sequence is

131 mainly defined by alternating quartzofeldspathic and mica-rich layers (Figure 2). Bottle-green

132 hornblende-rich metabasic mylonites, and purple-dark grey mylonites that are comparatively

133 mica rich are also present. Their presence reflects variations in protolith lithology (Cooper

134 and Norris, 2011; Norris and Cooper, 2007; Sibson et al., 1981; Toy, 2008). As the mylonites

135 in the hanging-wall are exhumed to depths of less than 8-12 km, temperatures drop below

136 those at which quartz plasticity occurs and brittle structures start to overprint the mylonitic

137 shear zone (Norris and Cooper, 2007; Toy et al., 2010, 2015). This brittle overprint is

138 reflected in the formation of a ~20 m thick layer of green, indurated and often foliated

139 cataclasite (Allen et al., 2017; Toy et al., 2015), and a 10-50 cm thick clay-rich PSZ that is

140 preserved adjacent to the currently-active fault trace (Boulton et al., 2017, 2012; Ikari et al.,

141 2014; Mitchell and Toy, 2014).

142

143 To the first-order (i.e. at scales >10 km), the trace of the Alpine Fault is remarkably linear,

144 with an average strike of 055º (Norris and Cooper, 2007). On the basis of geophysical

145 imaging and measurements of the mylonitic foliation -which is thought to parallel the fault- it

146 is estimated to dip at ~45º in its central section (Sibson et al., 1981; Stern et al., 2007), though

147 this may locally exceed 60º (Little et al., 2005; Toy et al., 2017). At scales of 1-10 km,

148 perturbations in the stress field induced by hanging-wall topography results in segmentation

149 of the Alpine Fault. Segmentation is rooted to depths of 0.5-4 km and comprises km-long,

150 approximately E-W striking and steeply-dipping strike-slip fault strands, which adjoin NE-

151 SW striking, gently-dipping (~30º) thrust segments (Barth et al., 2012; Langridge et al., 2014;

152 Norris and Cooper, 1995, 2007; Simpson et al., 1994; Upton et al., 2017).

3. Methods

3.1 Fracture orientations from DFDP-1 drill-core

Hanging-wall fracture orientations immediately adjacent to the Alpine Fault's PSZ were assessed through analysis of datasets arising from the first phase of the Deep Fault Drilling Project (DFDP-1, http://alpine.icdp-online.org). DFDP-1 successfully sampled the Alpine Fault in two boreholes (DFDP-1A and DFDP-1B, Figure 3) at depths of less than 150 m at Gaunt Creek (Figure 1b, Sutherland et al., 2012). The geophysical properties of the DFDP-1 boreholes were characterised by a full suite of wireline logs (Townend et al., 2013). These were combined with visual descriptions of ~70 m of core recovered across the two boreholes to construct a lithological classification scheme for DFDP-1 drill-core (Figure 3, Toy et al., 2015).

Abundant fractures were observed in X-ray computed tomography (CT) scans of DFDP-1 drill-core (Williams et al., 2016). The true orientations of these fracture were obtained by generating 'unrolled' CT images of individual core sections (Mills and Williams, 2017), which are directly analogous to geographically referenced - but lower resolution - borehole televiewer (BHTV) images. Where fractures could be matched between the two images, a rotation could be derived to transform all fracture orientations in the CT scans from a local core reference frame to their true geographic orientation (Figure 4). Depending on the number of fractures matched, core was rotated with a high, moderate, or low degree of confidence. In DFDP-1A, the quality of BHTV imaging was insufficient to attempt matching fractures, whereas in the Alpine Fault's relatively intact footwall (Townend et al., 2013), too few fractures (<1 fracture/core-section) could be imaged to attempt core reorientation. Therefore, the true orientation of fractures was only determined for the depth interval 94-126 m in the DFDP-1B borehole (Figure 3). Given the orientation of the PSZ-1 (which separates hanging-wall and footwall cataclasite) sampled in DFDP-1 (015/43 E; Townend et al., 2013), this

180 spans an orthogonal distance of ~25 m. A full methodology is provided in Appendix A, the

181 rotations applied to DFDP-1 core sections are listed in Table S1, and a complete CT-BHTV

182 image comparison is given in Williams et al. (2017b).

183

184 3.2 Field observations of fracture orientations and densities

185 At orthogonal distances of up to 150-250 m from the PSZs, fracture orientations and densities

186 were measured in four creeks (Gaunt Creek, Stony Creek, Hare Mare Creek and Havelock

187 Creek, Figure 1b) that cut across the hanging-wall sequence approximately perpendicular to

188 the main fault trace (Figure S1). Along each creek, fracture orientations and densities were

189 measured at 3 or 4 stations. This information was also gathered from approximately 500 m

190 from the Alpine Fault at Bullock Creek (Figure 1b). Each creek transect cuts across a thrust

191 segment of the Alpine Fault, so the orthogonal distance between the measuring stations and

192 the PSZs was calculated assuming a fault dip of 30º (Norris and Cooper, 1995, 1997). The

193 mylonite lithology for each station was classified using the scheme presented by Toy (2008).

194

195 The outcrops encountered along these transects are typically sub-vertical and may be covered

196 by debris except at their bases where they are frequently cleaned by flood events (Figure S2).

197 They are therefore poorly-suited for fracture density analysis using circular scanlines (e.g.

198 Mauldon et al., 2001). Instead, the fracture density was calculated from the number and

199 orientation of fractures that intersected a linear transect along the base of each outcrop (Priest,

200 1993; Schulz and Evans, 2000). This technique has the tendency to under-sample fractures

201 oriented at low angles to the scan-line. Therefore, a weighting (w) factor calculated using a

202 modified version of the Terzaghi correction (Massiot et al., 2015; Terzaghi, 1965) was

203 applied to each fracture, and results are shown as 'corrected' fracture density.

204

205 3.3 Fracture orientations in the Amethyst Hydro Project boreholes

206 The Amethyst Hydro Project (AHP) was developed to divert water from the Amethyst Ravine

207 down a 1040 m-long tunnel to a powerhouse on the floodplain of the Wanganui River. Prior

208 to the main phase of tunnelling, four exploratory boreholes (BH1-4; Figure 1b and S3) were

209 completed between 2005-2006, resulting in the recovery of ~890 m of drill-core at depths of

210 50-200 m. The boreholes are situated 1-2 km southeast of a thrust segment of the Alpine

211 Fault, where it may conceivably dip at a range of 30-60º (Norris and Cooper, 1995; Toy et al.,

212 2017). The drill-cores are therefore at orthogonal distances of ~0.7-2.0 km from the PSZs.

213

214 To provide a dataset analogous to the DFDP-1 CT scans, a total of 31.9 m of drill-core from

215 the AHP boreholes was CT scanned at the Southern Cross Hospital in Wellington, New

216 Zealand. Initial descriptions of the drill-core found that the Rock Quality Designation (RQD,

217 the % of intact core lengths >100 mm/1 m of drill-core) varied considerably due to intense

218 fracturing adjacent to the Tarpot Fault and other minor faults that intersect the AHP boreholes

219 (Geotech Consulting Limited, 2006; Savage, 2013). However, for practical reasons scanning

220 was focussed on intervals of high RQD (Figure S3). The CT scanner was operated at 100 mA

221 and an X-ray tube voltage of 120 kVp. Slice spacing was 1.25 mm, field of view 250 mm, and

222 the image size was 512 x 512 pixels. Therefore, the size of one voxel is 0.488 x 0.488 x 1.25

223 mm in the x, y, z directions respectively. Reconstruction of two-dimensional CT slices into

224 three-dimensional images of the drill-core was performed using OsiriX Imaging Software

225 (http://www.osirix-viewer.com/).

226

227 AHP drill-core was not oriented. However, the orientation of the schistosity is noted in the

228 drill-core logs to an accuracy of ±5° (Geotech Consulting Limited, 2006), where it is

229 consistent with the schistosity orientation measured in the Amethyst Tunnel itself (Savage,

230 2013). It can thus be used as a reference to reorient drill-core CT scans back into a geographic

231   reference frame. For BH2 and BH3 drill-cores, which are vertical, this required only a single

232   transformation. For the inclined BH1 and BH4 drill-cores, this required first rotating the core

233   with respect to the foliation. These orientations were then corrected for the inclination of the

234   drill core using the Planes from Oriented and Navigated Drillcore (POND) Excel spreadsheet

235   (Stanley and Hooper, 2003).

236   3.4 Statistical analysis of fracture orientations

237   The clustering intensity of fracture orientations was quantified using the resultant vector

238   method of Priest, (1993), where the vector for each fracture was weighted by the Terzaghi

239   correction for misorientation bias (Massiot et al., 2015; Terzaghi, 1965). This analysis was

240   performed only for the DFDP-1 and AHP datasets, which sampled a large population (>100)

241   of fractures. Field measuring stations sampled too few (<30) fractures to reliably perform this

242   analysis, and so their clustering is described in a qualitative sense only.

243   **4. Results**

244   4.1 Fracture orientations in DFDP-1 drill-core within 25 m of the Alpine Fault

245   In the DFDP-1 CT images, a total of 637 fractures were rotated into their true geographic

246   orientation where they show a weak cluster about the orientation of the foliation and Alpine

247   Fault PSZs at Gaunt Creek (015/43 E, Figures 5a, Appendix B; Townend et al., 2013).

248   Features in DFDP-1B BHTV images are also aligned about this orientation, but with a higher

249   cluster intensity than fractures noted in the CT images (Figure 5b, Table 1). This may reflect:

250   (1) features observed at the resolution of the BHTV are more likely to be aligned subparallel

251   to the fault plane and foliation than those visible in CT, and/or (2) some of the planar features

252   identified from the BHTV images were the mylonitic foliation itself. The clustering of

253   fractures hosted in foliated ultramylonites and cataclasites (Units 1, 2 and 4 of Toy et al.,

254   2015) is the same as fractures hosted in relatively homogenous unfoliated cataclasites (Unit 3

255 of Toy et al., 2015; Figures 5c and d, Table 1). We also observed no clear relationships

256 between fracture fill (Table 1 of Williams et al., 2016) and fracture orientation (Figure 5a).

257

258 4.2 Fracture orientations, densities, and fill in field transects within 500 m of the Alpine Fault

259 The orientations and densities of fractures observed in the four field transects are summarised

260 in Figure 7. In these transects, similar fractures to those observed in the CT scans of DFDP-1

261 core are identified (Figure 8). Total fracture density in the transects varies between 3-30

262 fractures/metre, and there is no clear decrease in fracture density with increasing distance

263 from the Alpine Fault in any of the transects (Figure 7a). Gouge-filled fractures (Figure 8a-c)

264 are observed at all distances from the Alpine Fault but are relatively abundant (>1

265 fracture/metre, Figure 7a, Table S2) within 100-160 m of the PSZs (Figure 7a). The thicker

266 gouge-filled fractures (>1 cm) commonly juxtapose different lithologies or offset markers

267 (Figure 8d-f). Thinner gouge-filled fractures (<1 cm) are localised to within 160 m of the

268 Alpine Fault. Open fractures (Figure 8g-i) are present at all stations, though are most

269 prevalent at those furthest from the fault (Figure 7b).

270

271 The composition of the mylonites can also affect fracture density. When they are juxtaposed

272 together, micaceous mylonites and ultramylonites are observed to contain relatively high

273 densities of gouge-filled fractures compared to quartzofeldspathic mylonites and

274 ultramylonites (Figures 9). Localities that showed the widest range in fracture orientations

275 tend to be less than 160 m from the PSZs within the ultramylonites (Figure 7b). Within

276 mylonite units, fracture orientations tend to be more aligned to the foliation (Figure 7b),

277 although gouge-filled fractures can sometimes cut across it (e.g. Bullock Creek).

278

279   4.3 Fractures in AHP drill-core, 0.7-2.0 km from the Alpine Fault

280   The AHP sampled grey, well-foliated Alpine Schist (Figure 10), a subgroup of the Haast

281   Schist (textural zone III-IV, Turnbull et al., (2001); Cox and Barrell., (2007)). Fracture

282   orientations are clustered about the orientation of the host rock schistosity in agreement with

283   the findings during initial drill-core descriptions and observations within the Amethyst

284   Tunnel itself (Figure 11; Geotech Consulting Limited, 2006; Savage, 2013). The clustering of

285   these fracture orientations is stronger than in the DFDP-1 datasets (Table 1). Fractures that

286   cut across the schistosity are most frequent in BH4 (Figure 10d and 11).

287

288   Though fractures are predominantly open, it is conceivable that the original fill may have

289   been lost during the subsequent core handling processes. This means that standard schemes to

290   differentiate between natural and induced fractures (Kulander et al., 1990; Williams et al.,

291   2016) cannot be applied to this dataset. Nevertheless, some open fractures must be natural as

292   they show alteration haloes (Figure 10a) implying that they were once conduits for fluid-flow.

293   Furthermore, packer tests conducted in these boreholes indicate hydraulic conductivities of

294    $\sim10^{-6}$-10^{-5} ms^{-1}, which is equivalent to permeabilities of 10^{-13}-10^{-12} m^2 (Cox et al., 2015;

295   Geotech Consulting Limited, 2006). No permeability measurements have been made in the

296   schist protolith at greater distances from Alpine Fault, however, these measurements are

297   orders of magnitude higher than has been reported in other metamorphic rock terranes ($\sim10^{-}$

298   ^{20}-10^{-17} m^2; Manning and Ingebritsen, 1999) and for typical continental crust ($\sim10^{-17}$ m^2;

299   Townend and Zoback, 2000).

300   **5 Discussion**

301   5.1 Fracture orientations in anisotropic wall rocks in the Alpine Fault hanging-wall

302   Two styles of fracturing are evident in the foliated Alpine Fault cataclasite, mylonite and

303   schist sequence (Figure 12). Within DFDP-1 drill-core, fractures are predominantly gouge-

304 filled and exhibit a range of orientations (Figure 5 and 6) with only a small proportion (11%)

305 of fractures in foliated cataclasites and ultramylonites clearly foliation-parallel (Williams et

306 al., 2016). However, in schists sampled by the AHP drill-core, the fractures are more

307 clustered about the foliation than in DFDP-1 drill-core (Figure 11, Table 1). The difference in

308 fracture clustering between the DFDP-1 and AHP drill-cores is qualitatively replicated by the

309 field transects, where fractures show variable orientations immediately adjacent to the Alpine

310 Fault but are typically foliation-parallel at the sites furthest from the fault (Figure 7).

311 Furthermore, field transects show that the variably oriented fractures have a gouge-fill, whilst

312 foliation-parallel fractures further from the fault tend to be open (Figures 7 and 8).

313

314 Experimental studies on foliated rocks demonstrate that mechanical anisotropy will exert the

315 greatest control on rock failure when: (1) the angle between the maximum principal stress

316 (σ_1) and the anisotropy (α) is ~30º, (2) confining pressure is low (<35 MPa), and (3) the

317 mechanical 'strength' of the anisotropy is high (Donath, 1961; Misra et al., 2015; Nasseri et

318 al., 2003; Paterson and Wong, 2005). The first factor can be approximated for the Alpine

319 Fault given the mylonite's average orientation of 055/45SE (Norris and Cooper, 2007) and

320 the stress tensor orientation within the surrounding crust, determined from focal mechanisms

321 of microseismicity in the fault's hanging-wall (Boese et al., 2012). This yields a value of α of

322 approximately 44º, when measured in the plane containing the maximum and minimum

323 principal stresses. This can be considered an intermediate value of α, since in deformation

324 experiments fractures may form parallel or non-parallel to the foliation depending on the

325 combination of confining pressure and lithology (Donath, 1961; Nasseri et al., 2003; Paterson

326 and Wong, 2005).

327

328 Foliation-parallel fractures are least common in the ultramylonites and foliated cataclasites.

329 Indeed, in the DFDP-1 datasets, there is no difference in fracture clustering between foliated

330 and unfoliated units (Table 1). Lithology may control mechanical anisotropy depending on

331 mineralogy, porosity, grain size, and the nature of the foliation surfaces (Donath, 1961;

332 Nasseri et al., 2003). It is notable that phase mixing and grain size reduction in the

333 ultramylonites reduces the intensity of the foliation, compared to the relatively coarse-grained

334 schists, protomylonites, and mylonites (Figure 2; Norris and Cooper, 2007; Toy et al., 2010,

335 2008). These data suggest that this lithological change could have a marked effect on the

336 orientation of fractures. Compositional variations between relatively quartzofeldspathic and

337 relatively micaceous mylonites can also influence the density of fractures (Figure 9). These

338 observations highlight that fracturing in the upper crust may be influenced by lithological

339 variations developed within an underlying linked, and synkinematic, shear zone. However, at

340 other localities (e.g. Stony Creek, Figure 7), variations in dominant fracture characteristics are

341 confined within units of similar composition and texture. This suggests that variations in

342 confining pressure may also be important in controlling the relationship between fractures and

343 foliation, as discussed in the next section.

344

345 5.2 Fracture damage around the Alpine Fault

346 Field transects across the Alpine Fault's hanging-wall show that fracture density remains

347 roughly constant (>3.5 fractures/m, corrected for orientation bias) for at least 500 m from the

348 fault (Figure 7a). Furthermore, the AHP (Cox et al., 2015) and DFDP-2B boreholes

349 (Sutherland et al., 2017; Townend et al., 2017) demonstrate an interval of enhanced

350 permeability (10^{-16}-10^{-13} m^2) that extends for at least 2 km into the Alpine Fault's hanging-

351 wall. Permeability in this rock mass is controlled by open fractures (Cox et al., 2015;

352 Sutherland et al., 2017; Townend et al., 2017) that are generally foliation-parallel (Massiot,

353 2017), and so directly analogous to the fractures sampled in the field (Figure 8g-i) and in

354 AHP drill-core (Figure 10). Conventional definitions of fault structure, that use fracture

355 density and permeability as criteria for damage zone width (e.g. Berg and Skar, 2005; Caine

356 et al., 1996; Faulkner et al., 2010; Savage and Brodsky, 2011; Schulz and Evans, 2000),

357 would therefore suggest that the Alpine Fault's damage zone extends for at least 500 m, and

358 possibly 2 km, into its hanging-wall.

359

360 Nevertheless, within the field transects we also note a distinct interval adjacent to the Alpine

361 Fault's PSZs that contains a relatively high density of gouge-filled fractures (>1

362 fracture/metre, Figure 7a). The width of this interval is <147 m (i.e. station 4) from the PSZs

363 at Gaunt Creek, <103 m at Stony Creek (i.e. station 3), <151 m at Hare Mare Creek (at station

364 2, Figure 8c) and <160 m at Havelock Creek (i.e. stations 4). These width estimates are based

365 on assumption that the Alpine Fault dips at 30° below the measuring stations (see the methods

366 section). However, the fault dip may locally vary (for example, the fault dip sampled by

367 DFDP-1 was 43°; Townend et al., (2013)), and there is also uncertainty in the depth extent of

368 its near-surface segmentation (Barth et al., 2012; Norris and Cooper, 1995; Upton et al.,

369 2017). Nevertheless, even if the fault dipped at 45° (Norris and Cooper, 2007) beneath the

370 measuring stations, the zone of higher-density gouge-filled fractures would be <205 m wide

371 (Table S3) and so is still appreciably closer to the Alpine Fault than the intervals sampled by

372 the AHP and DFDP-2 boreholes.

373

374 It is this ~100-160 m wide interval with a high density of gouge-filled fractures that Norris

375 and Cooper (1997, 2007) interpreted as the extent Alpine Fault's central section hanging-wall

376 damage zone. Furthermore, the width of this zone is comparable to damage zones widths

377 estimated elsewhere on the Alpine Fault (e.g. Barth et al., 2013 along the southern section;

378 Wright, 1998 at the northern end of the the central section, Figure 13a) and to other crustal-

379 scale fault zones that have accommodated hundreds of kilometres of displacement (Figure

380 13b; Faulkner et al., 2011; Savage and Brodsky, 2011).

381

382   Interpretations of damage zone width within the Alpine Fault's hanging-wall may therefore

383   differ by an order of magnitude depending on what criteria is used. To reconcile this,

384   Townend et al., (2017) suggested that the ~2 km wide interval of enhanced permeability and

385   foliation-parallel fracturing can be considered as an 'outer damage zone' (Figure 12).

386   Fractures within this zone may have formed by co-seismic shaking and slip on critically-

387   stressed fractures (Cox et al., 2015; Townend et al., 2017), or by the release of confining

388   pressure (Engelder, 1985; Price, 1959; Zangerl et al., 2006) during rapid exhumation (6-9

389   mm/yr) of the hanging-wall (Little et al., 2005; Tippett and Kamp, 1995). Rare gouge-filled

390   fractures (<1 fracture/metre) in this interval (e.g. Figure 8e) may also be the structures

391   accommodating the diffuse, low to moderate magnitude (M_W <6) seismicity that has been

392   recorded in a ~5 km wide zone within the Alpine Fault's hanging-wall (Boese et al., 2012;

393   Chamberlain et al., 2017; Eberhart-Phillips, 1995).

394

395   Conversely, the <160 m wide zone with a relatively high density of gouge-filled fractures

396   defines a narrower 'inner damage zone' (Figure 12; Townend et al. 2017). Microstructural

397   and compositional analysis of these fractures indicates that they formed in response to wear

398   and shearing of the wall rock and were subsequently mineralised due to circulation of

399   hydrothermal fluids (Warr and Cox, 2001; Williams et al., 2017a). Offset markers across

400   gouge-filled fractures (particularly those <1 cm thick) are rarely observed in DFDP-1 core

401   and field transects, but where they are present, reverse offset is most frequently noted (Figure

402   8d; Norris and Cooper, 1997; Toy et al., 2015). "Gouge-filled shears" that accommodated

403   strike-slip (Norris and Cooper, 1997), normal dip-slip (Cooper and Norris, 1994), or a

404   combination of both (Barth et al., 2012) have also been observed.

405

406   Cooper and Norris, (1994) interpreted that dip-slip fractures facilitated imbrication, tectonic

407   thickening and rotation of Alpine Fault thrust sheets as they moved across the irregular

408   topography of the footwall gravels. Dextral shears are interpreted to reflect the partitioning of

409 strike-slip movement away from shallowly dipping PSZs (Barth et al., 2012). The diverse

410 range of fracture orientations and shear senses in gouge-filled fractures therefore indicates

411 complex internal deformation of Alpine Fault thrust sheets in the near-surface (<500 m), as

412 they facilitate transpressional motion under the influence of km scale along-strike variations

413 in stress induced by the topography (Norris and Cooper, 1995; Upton et al., 2017).

414

415 Fractures may have also formed due to dynamic off-fault stresses (Ma, 2009; Rice et al.,

416 2005) during M_W >7.5 Alpine Fault earthquake ruptures (Sutherland et al., 2007). The

417 relatively thin seismogenic crust in the Alpine Fault's hanging-wall (10 ± 2 km, Boese et al.,

418 (2012)) will limit the generation of dynamic co-seismic damage to within ~100-200 m of the

419 fault (Ampuero and Mao, 2017). To the first order, this is comparable to the width of the

420 inner damage zone reported here.

421

422 5.3 Comparison to geophysical data

423 A 60-200 m wide low-velocity zone (LVZ) that extends to depths of ~8 km has been

424 documented around the Alpine Fault from the detection and character of Fault Zone Guided

425 Waves (FZGWs; Eccles et al., 2015). FZGWs are commonly regarded as an *in situ* indicator

426 of fault damage zone width (Ben-Zion and Sammis, 2003; Eberhart-Phillips et al., 1995;

427 Ellsworth and Malin, 2011; Li et al., 2014). Given the comparable widths of the Alpine Fault

428 LVZ (60-200 m) and the inner damage zone described here (100-160 m), we speculate that

429 the inner damage zone may trap FZGWs in the Alpine Fault hanging-wall. If this is true, it

430 implies that the inner damage zone extends to depths of ~8 km, consistent with the relatively

431 high-temperature (<400 °C) mineralising phases (calcite and chlorite) present in the gouge-

432 filled fractures (Williams et al., 2017a).

433

434 Though the boundary between the mylonites and ultramylonites is also ~100 m from the

435 Alpine Fault (Norris and Cooper, 2003; Toy et al., 2008), these two units have roughly

436 similar seismic velocities (Adam et al., 2016; Allen et al., 2017; Christensen and Okaya,

437 2007) and so are unlikely to channel FZGWs. We also note that since FZGWs are an

438 indicator of total fault zone width, our interpretation implies that most of the Alpine Fault's

439 LVZ is located in its hanging-wall. Western Province basement rocks to the west of the

440 Alpine Fault are rarely exposed (Lund Snee et al., 2014; Norris and Cooper, 2007), and so it

441 remains unknown if its footwall damage zone is indeed relatively narrow.

442 .

443 That the FZGWs are not being channelled by the margins of the ~2 km wide outer damage

444 zone leads us to conclude that this is a near-surface feature only (i.e. fractures are not kept

445 open at depth by pressurised fluids). If correct, this model of the Alpine Fault's hanging-wall

446 structure conforms to the expectations of fault zone flower structure models, which predict a

447 narrow inner damage zone that extends through the seismogenic crust, surrounded by a wider

448 zone of fractures in the near-surface at low confining pressures (~<3 km, Figure 12; e.g. Finzi

449 et al., 2009; Sylvester, 1988).

450

6. Conclusions

452 Fracture orientations and densities in the foliated hanging-wall of the Alpine Fault's central

453 section were quantified in drill-core from the Deep Fault Drilling Project (DFDP-1), field

454 transects in four creek sections, and drill-core recovered from the Amethyst Hydro Project. At

455 distances greater than approximately 160 m from the Alpine Fault principal slip zones (PSZs),

456 open and foliation-parallel fractures dominate. These are interpreted to form at low confining

457 pressures in mechanically anisotropic schist and mylonites. At distances less than ~160 m

458 from the PSZs, gouge-filled fractures with a wide range of orientations predominate. Fracture

459 density and orientation are locally influenced by changes in host rock lithology, but overall

460 fracture density is approximately constant at distances of up to ~500 m from the PSZs (Figure

461 12).

462

463 Following Townend et al., (2017), we interpret that the ~2 km wide zone of open foliation-

464 parallel fractures within the hanging-wall represents an "outer damage zone" that forms at

465 low confining pressures and relatively shallow depths. Conversely, the 160 m-wide zone of

466 gouge-filled fractures represents an "inner damage zone." The width of this zone is similar to

467 estimates for the low-velocity zone (LVZ) around the Alpine Fault made by Fault Zone

468 Guided Waves. We therefore interpret that the inner damage zone is the geological

469 manifestation of the LVZ, which if true, implies that the inner damage zone also extends to

470 depths of ~8 km. Overall, our interpretations are compatible with a flower structure model for

471 damage in the Alpine Fault's hanging-wall, with a relatively narrow zone of damage

472 extending towards the base of the seismogenic crust, which broadens upwards towards the

473 surface.

474 **Code availability**

475 The code to generate 'unrolled' circumferential CT images is available from the GFZ data

476 service (http://pmd.gfz-

477 potsdam.de/panmetaworks/review/7f1b114f11b67f540bb1360ead692dc578a66e3d0935c7fef

478 6ffe210db285300-icdp/).

479 **Data availability**

480 In the supplementary information, we include detailed field maps and cross sections (Figure

481 S1), photos of outcrops used for quantifying fracture density (Figure S2), a cross section

482 through the Amethyst Tunnel and location of boreholes (Figure S3), and an example of AHP

483 CT scans (Figure S4). The following tables are also provided, a list of rotations applied to

484 DFDP-1B core (Table S1), a summary of field transects including coordinates of the field

485 measuring stations (Table S2), and estimates of the distance of field measuring stations from

486 the Alpine Fault for different fault dips (Table S3). Lithological distribution and Alpine Fault

487 location as per University of Otago fault zone mapping program, which is available at:

488 http://www.otago.ac.nz/geology/research/structural-geology/alpine-fault/af-maps.html.

489 DFDP-1 and AHP CT scan 'core logs' and CT-BHTV image comparison are available on the

490 GFZ data service (http://pmd.gfz-

491 potsdam.de/panmetaworks/review/52b75045a30f1bd60f7fd5b841e69c468885e2a10dfc3704e

492 50b236df2ef8608-icdp).

493

494 **Acknowledgements**

495 DFDP-1 was funded by: GNS Science; Victoria University of Wellington; the University of

496 Otago; the University of Auckland; the University of Canterbury; Deutsche

497 Forschungsgemeinschaft and the University of Bremen; Natural Environment Research

498 Council grants NE/J024449/1, NE/ G524160/1 and NE/H012486/1 and the University of

499 Liverpool; and the Marsden Fund of the Royal Society of New Zealand. The International

500 Continental Scientific Drilling Program, ICDP (www.icdp-online.org) provided extensive

501 support. JW was supported by a University of Otago Doctoral Scholarship. We thank

502 Matthew Parris at the Oncology Department at Dunedin Hospital, and Darren Tod at the

503 Southern Cross Hospital, Wellington, for support in collecting CT scans of DFDP-1 Amethyst

504 Hydro Project drill-core respectively. Katrina Sauer, Ben Melosh and Astrid Vetrhus

505 provided field assistance. Comments by Tim Little and Tom Blenkinsop, and by two

506 anonymous reviewers on an earlier version of this manuscript, improved this paper.

507 **Appendix A: DFDP-1B core rotation methodology**

508 The technique employed to reorient core DFDP-1 here is similar to that described in Jarrard et

509 al., (2001), Paulsen et al., (2002) and Shigematsu et al., (2014), however, instead of

510 comparing DFDP-1 BHTV data to DMT CoreScan system® unrolled core scans, we compare

511 BTHV images to 'unrolled' CT core images. The acquisition and interpretation of the DFDP-

512 1 BHTV logs has been previously described by Townend et al., (2013) and McNamara,

513 (2015). DFDP-1 CT scans consist of a stack of core-axial perpendicular image slices with a

514 pixel size of 0.244 mm and a spacing of 1 mm. The CT stack for each core section was loaded

515 into Fiji (http://fiji.sc/Fiji) and a circle was manually defined around the irregular boundary of

516 drill-core in a core axial-perpendicular image slice using the code available at Mills and

517 Williams, (2017). This circle was then used to define the path of the image in all other slices.

518 Generation of the unrolled images accounts for the fact that the spacing between individual

519 CT slices (1 mm, i.e. the core-axial parallel pixel size) is greater than the pixel size within the

520 slices (0.244 mm). Unrolled images were then reflected around the borehole axis as an image

521 of the outer surface of the core and a BHTV image are reflections of each other. This

522 technique has benefits over methods using the DMT CoreScan system®, since drill-core does

523 not have to be physically rotated and so can be used without the risk of damaging fragile core

524 sections.

525

526 Unrolled CT images were imported into the composite log viewing software WellCAD®

527 (http://www.alt.lu/wellcad.htm) along with the BHTV images, where they are placed side-by-

528 side to allow matching of structures (Figure 4, see also Williams et al., (2017b)). When

529 correlating the two datasets, it was first necessary to account for possible depth shifts between

530 recorded drill-core depths and BHTV imagery due to factors such as stretching of the logging

531 cable and intervals from which no drill-core was recovered (Haggas et al., 2001; Jarrard et al.,

532 2001). In this study, a depth shift of no more than ±30 cm was allowed.

533

534 The orientation of fractures in the DFDP-1 CT images had previously been measured within a

535 local core reference frame (see Figure 4 in Williams et al., 2016). Since the DFDP-1

536 boreholes were vertical, corrections to reorient the drill-core back into a geographic reference

537   frame required only a single rotation about the core axis to correct for the dip direction. When

538   correlating structures, errors may be introduced by: (1) the internal BHTV magnetometer

539   ($\pm2°$), (2) the manual picking of sinusoidal curves on BHTV and unrolled CT images that can

540   be $\pm10°$ for shallowly dipping ($<30°$) structures (Jarrard et al., 2001), and (3) the fact that the

541   DFDP-1B BHTV data imaged the open borehole, which has a larger diameter (127 mm) than

542   the drill-core (85 mm). To mitigate against the cumulative effect of these errors, Jarrard et al.,

543   (2001) stitched unrolled images of many different core sections together that spanned

544   intervals of 5-30 m, prior to the matching with BHTV imagery. This meant that only a single

545   rotation was necessary for all core sections across the entire stitched interval, which could be

546   based on identifying ~20-30 matching structures between the BHTV and unrolled core

547   images.

548

549   In DFDP-1 it was not possible to stitch unrolled CT images of core section together as no

550   prominent reference marker across different sections were identified. Consequently each <1

551   m long core section had to be reoriented individually, within which we never identified more

552   than 3 matching structures. Therefore, compared to the methodology described by Jarrard et

553   al., (2001), the degree of confidence on the applied reorientation was strongly dependent on

554   the quality of individual matches for each core section and the range of rotations that they

555   indicated. We recorded this qualitatively for each core section using the scheme outlined

556   below.

557

558   • High degree of confidence: images matched with one very prominent structure (e.g.

559   Figure 4d), or matched with two or more structures whose range of suggested

560   rotations are within 10° of each other (Figure 4b and c).

561

Deleted: Figure 4

Deleted: Figure 4

564 • Moderate degree of confidence: images matched with one prominent feature or two

565 features that indicate rotations that range 10-19° (e.g. Figure 4a) or three features

566 whose range of suggested rotations are within 20-30° of each other.

567

568 • Low degree of confidence: images matched with one feature or two features whose

569 range of suggested rotations are within 20-30° of each other.

570

571 In this scheme, a core reorientation is deemed unreliable if the range of rotations suggested by

572 different structures is ≥30°, i.e. equivalent to the cumulative effect of possible errors listed

573 above. For those core sections where more than one matching structure was identified, the

574 rotation that was applied was derived from the average of that required for each match. If one

575 of the matched structures was more prominent, then the applied rotation was biased towards

576 that structure.

577

578 **Appendix B: DFDP-1B core rotation validity**

579 Based on the criteria presented in Appendix A, of the 40 core sections from DFDP-1B in

580 which there was suitable quality of unrolled CT and BHTV images to attempt reorientation

581 (Figure 3), 31 were reoriented (Table S1). Prior to reorientation, fractures in these sections

582 exhibit no clustering (Figure A1a), however, a weak one does develop after reorientation

583 (Figure 5a). Since fractures in nature typically exhibit non-random orientations, this is

584 evidence that the reorientation of the CT scans was successful (Kulander et al., 1990; Paulsen

585 et al., 2002). In addition, fractures within some individual core sections (Figure A1b), and

586 fractures rotated based on a high degree of confidence (Figure A1c) contain a wide range of

587 orientations.

588

The recognition of fractures in unrolled CT images that are not observed in BHTV can be readily explained by the higher resolution of the CT images. However, structures are also observed in the BHTV logs, but not interpreted as fractures in the CT images (Figure 4). This may represent noise in the BHTV images, or in the case of foliation-parallel structures, the ultramylonitic foliation itself since it can be difficult to differentiate these structures. The subordinate north-dipping set of fractures in the BHTV images (Figure 5b) is not recognised in the orientations gathered from CT images (Figure 5a). A similar north dipping fracture set was also recognised in DFDP-2B BHTV images (Massiot 2017), and their causation and relevance is the focus of ongoing work.

Competing Interests

Authors declare that they have no conflict of interest.

References

Adam, L., Toy, V. and Boulton, C.: Mylonites as shales? Experimental observations of P-wave anisotropy dependence on mineralogy, layering and scale, in SEG Technical Program Expanded Abstracts 2016, pp. 3169–3173, Society of Exploration Geophysicists., 2016.

Allen, M. J., Tatham, D., Faulkner, D. R., Mariani, E. and Boulton, C.: Permeability and seismic velocity and their anisotropy across the Alpine Fault, New Zealand: An insight from laboratory measurements on core from the Deep Fault Drilling Project phase 1 (DFDP-1), J. Geophys. Res. Solid Earth, 122(8), 6160–6179, doi:10.1002/2017JB014355, 2017.

Ampuero, J. P. and Mao, X.: Upper limit on damage zone thickness controlled by seismogenic depth, Fault Zo. Dyn. Process. Evol. Fault Prop. Dur. Seism. Rupture, 227, 243, 2017.

Andrews, D. J.: Rupture dynamics with energy loss outside the slip zone, J. Geophys. Res. Solid Earth, 110(1), 1–14, doi:10.1029/2004JB003191, 2005.

614 Barth, N. C., Toy, V. G., Langridge, R. M. and Norris, R. J.: Scale dependence of oblique

615 plate-boundary partitioning: New insights from LiDAR, central Alpine fault, New Zealand,

616 Lithosphere, 4(5), 435–448, doi:10.1130/L201.1, 2012.

617 Barth, N. C., Boulton, C., Carpenter, B. M., Batt, G. E. and Toy, V. G.: Slip localization on

618 the southern Alpine Fault New Zealand, Tectonics, 32(3), 620–640, doi:10.1002/tect.20041,

619 2013.

620 Ben-Zion, Y. and Sammis, C. G.: Characterization of Fault Zones, Pure Appl. Geophys.,

621 160(3), 677–715, doi:10.1007/PL00012554, 2003.

622 Berg, S. S. and Skar, T.: Controls on damage zone asymmetry of a normal fault zone:

623 Outcrop analyses of a segment of the Moab fault, SE Utah, J. Struct. Geol., 27(10), 1803–

624 1822, doi:10.1016/j.jsg.2005.04.012, 2005.

625 Bistacchi, A., Massironi, M. and Menegon, L.: Three-dimensional characterization of a

626 crustal-scale fault zone: The Pusteria and Sprechenstein fault system (Eastern Alps), J. Struct.

627 Geol., 32(12), 2022–2041, doi:10.1016/j.jsg.2010.06.003, 2010.

628 Bistacchi, A., Massironi, M., Menegon, L., Bolognesi, F. and Donghi, V.: On the nucleation

629 of non-Andersonian faults along phyllosilicate-rich mylonite belts, Geol. Soc. London, Spec.

630 Publ., 367(1), 185–199, doi:10.1144/sp367.13, 2012.

631 Boese, C. M. M., Townend, J., Smith, E. and Stern, T.: Microseismicity and stress in the

632 vicinity of the Alpine Fault, central Southern Alps, New Zealand, J. Geophys. Res. Solid

633 Earth, 117(2), doi:10.1029/2011JB008460, 2012.

634 Boulton, C., Yao, L., Faulkner, D. R., Townend, J., Toy, V. G., Sutherland, R., Ma, S. and

635 Shimamoto, T.: High-velocity frictional properties of Alpine Fault rocks: Mechanical data,

636 microstructural analysis, and implications for rupture propagation, J. Struct. Geol., 97, 71–92,

637 doi:10.1016/j.jsg.2017.02.003, 2017.

638 Boulton, C. J., Carpenter, B. M., Toy, V. and Marone, C.: Physical properties of surface

639 outcrop cataclastic fault rocks, Alpine Fault, New Zealand, Geochemistry, Geophys.

640   Geosystems, 13(1), doi:10.1029/2011GC003872, 2012.

641   Caine, J. S., Evans, J. P. and Forster, C. B.: Fault zone architecture and permeability structure,

642   Geology, 24(11), 1025–1028, 1996.

643   Chamberlain, C. J., Boese, C. M. and Townend, J.: Cross-correlation-based detection and

644   characterisation of microseismicity adjacent to the locked, late-interseismic Alpine Fault,

645   South Westland, New Zealand, Earth Planet. Sci. Lett., 457, 63–72,

646   doi:10.1016/j.epsl.2016.09.061, 2017.

647   Chester, F. M. and Chester, J. S.: Stress and deformation along wavy frictional faults, J.

648   Geophys. Res., 105(B10), 23421, doi:10.1029/2000JB900241, 2000.

649   Chester, F. M. and Logan, J. M.: Implications for mechanical properties of brittle faults from

650   observations of the Punchbowl fault zone, California, Pure Appl. Geophys. PAGEOPH,

651   124(1–2), 79–106, doi:10.1007/BF00875720, 1986.

652   Chester, F. M., Evans, J. P. and Biegel, R. L.: Internal structure and weakening mechanisms

653   of the San Andreas Fault, J. Geophys. Res., 98(B1), 771, doi:10.1029/92JB01866, 1993.

654   Chester, J. S. and Fletcher, R. C.: Stress distribution and failure in anisotropic rock near a

655   bend on a weak fault, J. Geophys. Res. Earth, 102(B1), 693–708, doi:10.1029/96JB02791,

656   1997.

657   Choi, J. H., Edwards, P., Ko, K. and Kim, Y. S.: Definition and classification of fault damage

658   zones: A review and a new methodological approach, Earth-Science Rev., 152, 70–87,

659   doi:10.1016/j.earscirev.2015.11.006, 2016.

660   Christensen, N. I. and Okaya, D. A.: Compressional and shear wave velocities in South

661   Island, New Zealand rocks and their application to the interpretation of seismological models

662   of the New Zealand crust, A Cont. Plate Bound. Tectonics South Island, New Zeal., 123–155,

663   2007.

664   Columbus, J., Sirguey, P. and Tenzer, R.: A free, fully assessed 15-m DEM for New Zealand,

665   Surv. Q., 66(66), 16–19, 2011.

666   Cooper, A. F. and Norris, R. J.: Anatomy, structural evolution, and slip rate of a plate-

667   boundary thrust: the Alpine Fault at Gaunt Creek, Westland, New Zealand, Geol. Soc. Am.

668   Bull., 106(5), 627–633, doi:10.1130/0016-7606(1994)106<0627:ASEASR>2.3.CO;2, 1994.

669   Cooper, A. F. and Norris, R. J.: Inverted metamorphic sequences in Alpine fault mylonites

670   produced by oblique shear within a plate boundary fault zone, New Zealand., 2011.

671   Cowie, P. A. and Scholz, C. H.: Physical Explanation for the Displacement Length

672   Relationship of Faults Using a Post-Yield Fracture-Mechanics Model, J. Struct. Geol., 14(10),

673   1133–1148, doi:10.1016/0191-8141(92)90065-5, 1992.

674   Cox, S. C., Menzies, C. D., Sutherland, R., Denys, P. H., Chamberlain, C. and Teagle, D. A.

675   H.: Changes in hot spring temperature and hydrogeology of the Alpine Fault hanging wall,

676   New Zealand, induced by distal South Island earthquakes, Geofluids, 15(1–2), 216–239,

677   2015.

678   DeMets, C., Gordon, R. G., Argus, D. F. and Stein, S.: Effect of recent revisions to the

679   geomagnetic reversal time scale on estimate of current plate motions, Geophys. Res. Lett.,

680   21(20), 2191–2194, doi:10.1029/94GL02118, 1994.

681   Donath, F. A.: Experimental study of shear failure in anisotropic rocks, Geol. Soc. Am. Bull.,

682   72(6), 985–989, doi:10.1130/0016-7606(1961)72[985:ESOSFI]2.0.CO;2, 1961.

683   Eberhart-Phillips, D., Stanley, W. D., Rodriguez, B. D. and Lutter, W. J.: Surface seismic and

684   electrical methods to detect fluids related to faulting, J. Geophys. Res., 100(B7), 12919–

685   12936, doi:10.1029/94JB03256, 1995.

686   Eberhart-Phillips, D.: Examination of seismicity in the central Alpine fault region, South

687   Island, New Zealand, New Zeal. J. Geol. Geophys., 38(4), 571–578, 1995.

688   Eccles, J. D., Gulley, A. K., Malin, P. E., Boese, C. M., Townend, J. and Sutherland, R.: Fault

689   Zone Guided Wave generation on the locked, late interseismic Alpine Fault, New Zealand,

690   Geophys. Res. Lett., 42(14), 5736–5743, doi:10.1002/2015GL064208, 2015.

691   Ellsworth, W. L. and Malin, P. E.: Deep rock damage in the San Andreas Fault revealed by P-

692   and S-type fault-zone-guided waves, Fagereng, A., Toy, V.G., Rowland, J. (Eds), Geol.

693   Earthq. Source A Vol. Honor Rick Sibson, Geol. Soc. London, Spec. Publ., 359(1), 39–53,

694   doi:10.1144/SP359.3, 2011.

695   Engelder, T.: Loading paths to joint propagation during a tectonic cycle: an example from the

696   Appalachian Plateau, U.S.A., J. Struct. Geol., 7(3–4), 459–476, doi:10.1016/0191-

697   8141(85)90049-5, 1985.

698   Faulkner, D. R., Jackson, C. A. L., Lunn, R. J., Schlische, R. W., Shipton, Z. K., Wibberley,

699   C. A. J. and Withjack, M. O.: A review of recent developments concerning the structure,

700   mechanics and fluid flow properties of fault zones, J. Struct. Geol., 32(11), 1557–1575,

701   doi:10.1016/j.jsg.2010.06.009, 2010.

702   Faulkner, D. R., Mitchell, T. M., Jensen, E. and Cembrano, J.: Scaling of fault damage zones

703   with displacement and the implications for fault growth processes, J. Geophys. Res. Solid

704   Earth, 116(5), doi:10.1029/2010JB007788, 2011.

705   Finzi, Y., Hearn, E. H., Ben-Zion, Y. and Lyakhovsky, V.: Structural properties and

706   deformation patterns of evolving strike-slip faults: Numerical simulations incorporating

707   damage rheology, Pure Appl. Geophys., 166(10–11), 1537–1573, doi:10.1007/s00024-009-

708   0522-1, 2009.

709   Geotech Consulting Limited: Amethyst Hydro Scheme Drilling Investigation Summary

710   Report., 2006.

711   Haggas, S., Brewer, T. S., Harvey, P. K. and Iturrino, G. I.: Relocating and orientating cores

712   by the integration of electrical and optical images, J. Geol. Soc. London, 158, 615–623,

713   doi:10.1144/jgs.158.4.615, 2001.

714   Ikari, M. J., Carpenter, B. M., Kopf, A. J. and Marone, C.: Frictional strength, rate-

715   dependence, and healing in DFDP-1 borehole samples from the Alpine Fault, New Zealand,

716   Tectonophysics, 630(C), 1–8, doi:10.1016/j.tecto.2014.05.005, 2014.

717   Jarrard, R. D., Paulsen, T. S. and Wilson, T. J.: Orientation of CRP-3 core, Victoria Land

718   Basin, Antarctica, Terra Antarct., 8(3), 161–166, 2001.

719   Kim, Y. S. and Sanderson, D. J.: Fault propagation, displacement and damage zones, Struct.

720   Geol. New Res., 1, 99–117, 2008.

721   Kim, Y. S., Peacock, D. C. P. and Sanderson, D. J.: Fault damage zones, J. Struct. Geol.,

722   26(3), 503–517, doi:10.1016/j.jsg.2003.08.002, 2004.

723   Kulander, B. R., Dean, S. L. and Ward, B. J.: Fracture core analysis: interpretation, logging

724   and use of natural and induced fractures in core, American Association of Petroleum

725   Geologists., 1990.

726   Langridge, R. M., Ries, W. F., Farrier, T., Barth, N. C., Khajavi, N. and De Pascale, G. P.:

727   Developing sub 5-m LiDAR DEMs for forested sections of the Alpine and Hope faults, South

728   Island, New Zealand: Implications for structural interpretations, J. Struct. Geol., 64, 53–66,

729   doi:10.1016/j.jsg.2013.11.007, 2014.

730   Lees, J. M.: RFOC: Graphics for spherical distributions and earthquake focal mechanisms. R

731   package version 3.3-3. http://CRAN.R-project.org/package=RFOC, R Packag. version, 3(2),

732   2014.

733   Li, Y. G., De Pascale, G. P., Quigley, M. C. and Gravley, D. M.: Fault damage zones of the

734   M7.1 Darfield and M6.3 Christchurch earthquakes characterized by fault-zone trapped waves,

735   Tectonophysics, 618, 79–101, doi:10.1016/j.tecto.2014.01.029, 2014.

736   Little, T. A., Cox, S., Vry, J. K. and Batt, G.: Variations in exhumation level and uplift rate

737   along the obliqu-slip Alpine fault, central Southern Alps, New Zealand, Geol. Soc. Am. Bull.,

738   117(5), 707, doi:10.1130/B25500.1, 2005.

739   Lund Snee, J. E., Toy, V. G. and Gessner, K.: Significance of brittle deformation in the

740   footwall of the Alpine Fault, New Zealand: Smithy Creek Fault zone, J. Struct. Geol., 64, 79–

741   98, doi:10.1016/j.jsg.2013.06.002, 2014.

742   Ma, S.: Distinct asymmetry in rupture-induced inelastic strain across dipping faults: An off-

743   fault yielding model, Geophys. Res. Lett., 36(20), doi:10.1029/2009GL040666, 2009.

744   Manning, C. E. and Ingebritsen, S. E.: Permeability of the continental crust: Implications of

745   geothermal data and metamorphic systems, Rev. Geophys., 37(1), 127–150,

746   doi:10.1029/1998RG900002, 1999.

747   Massiot, C.: Fracture system characterisation and implications for fluid flow in volcanic and

748   metamorphic rocks, , 1–191, 2017.

749   Massiot, C., Mcnamara, D. D. and Lewis, B.: Geothermics Processing and analysis of high

750   temperature geothermal acoustic borehole image logs in the Taupo Volcanic Zone , New

751   Zealand, Geothermics, 53, 190–201, doi:10.1016/j.geothermics.2014.05.010, 2015.

752   Massironi, M., Bistacchi, A. and Menegon, L.: Misoriented faults in exhumed metamorphic

753   complexes: Rule or exception?, Earth Planet. Sci. Lett., 307(1–2), 233–239,

754   doi:10.1016/j.epsl.2011.04.041, 2011.

755   Mauldon, M., Dunne, W. M. and Rohrbaugh, M. B.: Circular scanlines and circular windows:

756   New tools for characterizing the geometry of fracture traces, J. Struct. Geol., 23(2–3), 247–

757   258, doi:10.1016/S0191-8141(00)00094-8, 2001.

758   McNamara, D.: Exploring New Zealand's subsurface using borehole images, in Presented at

759   the 2015 New Zealand Geosciences Conference, Wellington, 25-27th November (2015).,

760   2015.

761   Mills, S. and Williams, J. N.: Generating circumferential images of tomographic drill-core

762   scans, GFZ Data Serv., doi:http://doi.org/10.5880/ICDP.5052.005, 2017.

763   Misra, S., Ellis, S. and Mandal, N.: Fault damage zones in mechanically layered rocks: The

764   effects of planar anisotropy, J. Geophys. Res. B Solid Earth, 120(8), 5432–5452,

765   doi:10.1002/2014JB011780, 2015.

766   Mitchell, T. M. and Faulkner, D. R.: The nature and origin of off-fault damage surrounding

767   strike-slip fault zones with a wide range of displacements: A field study from the Atacama

768   fault system, northern Chile, J. Struct. Geol., 31(8), 802–816, doi:10.1016/j.jsg.2009.05.002,

769   2009.

770   Mitchell, T. M. and Toy, V. G.: Photograph of the month, J. Struct. Geol., 61, 143,

771   doi:10.1016/j.jsg.2014.01.004, 2014.

772   Muir-Wood, R. and King, G. C. P.: Hydrological signatures of earthquake strain, J. Geophys.

773   Res., 98(B12), 22035, doi:10.1029/93JB02219, 1993.

774   Nasseri, M. H. B., Rao, K. S. and Ramamurthy, T.: Anisotropic strength and deformation

775   behavior of Himalayan schists, Int. J. Rock Mech. Min. Sci., 40(1), 3–23, doi:10.1016/S1365-

776   1609(02)00103-X, 2003.

777   Norris, R. J. and Cooper, A. F.: Origin of small-scale segmentation and transpressional

778   thrusting along the Alpine Fault, New Zealand, Geol. Soc. Am. Bull., 107(2), 231–240,

779   doi:10.1130/0016-7606(1995)107<0231:OOSSSA>2.3.CO;2, 1995.

780   Norris, R. J. and Cooper, A. F.: Erosional control on the structural evolution of a

781   transpressional thrust complex on the Alpine fault, New Zealand, J. Struct. Geol., 19(10),

782   1323–1342, doi:10.1016/S0191-8141(97)00036-9, 1997.

783   Norris, R. J. and Cooper, A. F.: Late Quaternary slip rates and slip-partitioning on the Alpine

784   Fault, New Zealand, J. Struct. Geol., 23(2000), 507–520, 2001.

785   Norris, R. J. and Cooper, A. F.: Very high strains recorded in mylonites along the Alpine

786   Fault, New Zealand: implications for the deep structure of plate boundary faults, J. Struct.

787   Geol., 25(12), 2141–2157, 2003.

788   Norris, R. J. and Cooper, A. F.: The Alpine Fault, New Zealand: Surface Geology and Field

789   Relationships, in A Continental Plate Boundary: Tectonics at South Island, New Zealand,

790   edited by D. Okaya, T. A. Stern, and F. Davey, pp. 157–175, American Geophysical Union.,

791   2007.

792   Norris, R. J. and Toy, V. G.: Continental transforms: A view from the Alpine Fault, J. Struct.

793   Geol., 64, 3–31, doi:10.1016/j.jsg.2014.03.003, 2014.

794   O'Brien, G. A., Cox, S. C. and Townend, J.: Spatially and temporally systematic hydrologic

795   changes within large geoengineered landslides, Cromwell Gorge, New Zealand, induced by

796   multiple regional earthquakes, J. Geophys. Res. Solid Earth, 121(12), 8750–8773, 2016.

797   Paterson, M. S. and Wong, T. F.: Experimental rock deformation - The brittle field, Springer-

798   Verlag Berlin Heidelberg., 2005.

799   Paulsen, T. S., Jarrard, R. D. and Wilson, T. J.: A simple method for orienting drill core by

800   correlating features in whole-core scans and oriented borehole-wall imagery, J. Struct. Geol.,

801   24(8), 1233–1238, doi:10.1016/S0191-8141(01)00133-X, 2002.

802   Peacock, D. C. P. and Sanderson, D. J.: Effects of layering and anisotropy on fault geometry,

803   J. Geol. Soc. London., 149(5), 793–802, doi:10.1144/gsjgs.149.5.0793, 1992.

804   Price, N. J.: Mechanics of jointing in rocks, Geol. Mag., 96(2), 149–167,

805   doi:10.1017/S0016756800060040, 1959.

806   Priest, S.: Discontinuity Analysis for Rock Engineering, Springer Science & Business Media.,

807   1993.

808   Rattenbury, M. and Isaac, M.: The QMAP 1:250 000 Geological Map of New Zealand

809   project, New Zeal. J. Geol. Geophys., 8306(April), doi:10.1080/00288306.2012.725417,

810   2012.

811   Reed, J. J.: Mylonites, cataclasites, and associated rocks along the Alpine fault, South Island,

812   New Zealand, New Zeal. J. Geol. Geophys., 7(4), 645–684,

813   doi:10.1080/00288306.1964.10428124, 1964.

814   Rice, J. R., Sammis, C. G. and Parsons, R.: Off-fault secondary failure induced by a dynamic

815   slip pulse, Bull. Seismol. Soc. Am., 95(1), 109–134, doi:10.1785/0120030166, 2005.

816   Savage, E.: Investigating Rock Mass Conditions and Implications for Tunnelling and

817 Construction of the Amethyst Hydro Project, Harihari, University of Canterbury., 2013.

818 Savage, H. M. and Brodsky, E. E.: Collateral damage: Evolution with displacement of

819 fracture distribution and secondary fault strands in fault damage zones, J. Geophys. Res. Solid

820 Earth, 116(3), doi:10.1029/2010JB007665, 2011.

821 Savage, H. M., Keranen, K. M., Schaff, D. and Dieck, C.: Possible Precursory Signals in

822 Damage Zone Foreshocks, Geophys. Res. Lett., 2017.

823 Schulz, S. E. and Evans, J. P.: Mesoscopic structure of the Punchbowl Fault, Southern

824 California and the geologic and geophysical structure of active strike-slip faults, J. Struct.

825 Geol., 22(7), 913–930, doi:10.1016/S0191-8141(00)00019-5, 2000.

826 Shigematsu, N., Otsubo, M., Fujimoto, K. and Tanaka, N.: Orienting drill core using

827 borehole-wall image correlation analysis, J. Struct. Geol., 67(PB), 293–299,

828 doi:10.1016/j.jsg.2014.01.016, 2014.

829 Sibson, R. H.: Earthquake faulting as a structural process, J. Struct. Geol., 11(1–2), 1–14,

830 doi:10.1016/0191-8141(89)90032-1, 1989.

831 Sibson, R. H., White, S. H. and Atkinson, B. K.: Structure and distribution of fault rocks in

832 the Alpine Fault Zone, New Zealand, Geol. Soc. London, Spec. Publ., 9(1), 197–210, 1981.

833 Simpson, G. D. H., Cooper, A. F. and Norris, R. J.: Late Quaternary evolution of the Alpine

834 Fault Zone at Paringa, South Westland, New Zealand, New Zeal. J. Geol. Geophys., 37(1),

835 49–58, doi:10.1080/00288306.1994.9514600, 1994.

836 Stanley, C. R. and Hooper, J. J.: POND: An Excel spreadsheet to obtain structural attitudes of

837 planes from oriented drillcore, Comput. Geosci., 29(4), 531–537, doi:10.1016/S0098-

838 3004(03)00033-5, 2003.

839 Stern, T., Okaya, D., Kleffmann, S., Scherwath, M., Henrys, S. and Davey, F.: Geophysical

840 exploration and dynamics of the Alpine Fault Zone, A Cont. Plate Bound. Tectonics South

841 Island, New Zeal. Geophys. Monogr. Ser. 175, 207–233, doi:10.1029/175GM11, 2007.

842 Sutherland, R., Eberhart-Phillips, D., Harris, R. A., Stern, T., Beavan, J., Ellis, S., Henrys, S.,

843 Cox, S., Norris, R. J., Berryman, K. R., Townend, J., Bannister, S., Pettinga, J., Leitner, B.,

844 Wallace, L., Little, T. A., Cooper, A. F., Yetton, M. and Stirling, M.: Do Great Earthquakes

845 Occur on the Alpine Fault in Central South Island, New Zealand?, in A Continental Plate

846 Boundary: Tectonics at South Island, New Zealand, vol. 175, edited by D. Okaya, Stern, T.,

847 and F. Davey, pp. 235–251, American Geophysical Union., 2007.

848 Sutherland, R., Toy, V. G., Townend, J., Cox, S. C., Eccles, J. D., Faulkner, D. R., Prior, D.

849 J., Norris, R. J., Mariani, E., Boulton, C., Carpenter, B. M., Menzies, C. D., Little, T. A.,

850 Hasting, M., De Pascale, G. P., Langridge, R. M., Scott, H. R., Reid Lindroos, Z., Fleming, B.

851 and Kopf, J.: Drilling reveals fluid control on architecture and rupture of the Alpine fault,

852 New Zealand, Geology, 40(12), 1143–1146, doi:10.1130/G33614.1, 2012.

853 Sutherland, R., Townend, J., Toy, V. G., Upton, P., Coussens, J. and DFDP2, S. T.: Extreme

854 hydrothermal conditions at an active plate-bounding fault, Nature, 546, 137–140,

855 doi:10.1038/nature22355, 2017.

856 Sylvester, A. G.: Strike-Slip Faults, Geol. Soc. Am. Bull., 100(November), 1666–1703,

857 doi:10.1130/0016-7606(1988)100<1666:SSF>2.3.CO;2, 1988.

858 Templeton, E. L., Rice, J. R., Viesca, R. C., Templeton, E. L. and Rice, J. R.: Off-fault

859 plasticity and earthquake rupture dynamics: 2. Effects of fluid saturation, J. Geophys. Res.

860 Solid Earth, 113(9), doi:10.1029/2007JB005530, 2008.

861 Terzaghi, R. D.: Sources of Error in Joint Surveys, Géotechnique, 15(3), 287–304,

862 doi:10.1680/geot.1965.15.3.287, 1965.

863 Tippett, J. M. and Kamp, P. J. J.: Quantitative relationships between uplift and relief

864 parameters for the Southern Alps, New Zealand, as determined by fission track analysis,

865 Earth Surf. Process. Landforms, 20(2), 153–175, 1995.

866 Townend, J. and Zoback, M. D.: How faulting keeps the crust strong, Geology, 28(5), 399–

867 402, doi:10.1130/0091-7613(2000)28<399:HFKTCS>2.0.CO, 2000.

868 Townend, J., Sutherland, R., Toy, V. G., Eccles, J. D., Boulton, C., Cox, S. C. and

869 McNamara, D.: Late-interseismic state of a continental plate-bounding fault: Petrophysical

870 results from DFDP-1 wireline logging and core analysis, Alpine Fault, New Zealand,

871 Geochemistry, Geophys. Geosystems, 14(9), 3801–3820, doi:10.1002/ggge.20236, 2013.

872 Townend, J., Sutherland, R., Toy, V. G., Doan, M. L., Célérier, B., Massiot, C., Coussens, J.,

873 Jeppson, T., Janku-Capova, L., Remaud, L., Upton, P., Schmitt, D. R., Pezard, P., Williams,

874 J., Allen, M. J., Baratin, L. M., Barth, N., Becroft, L., Boese, C. M., Boulton, C., Broderick,

875 N., Carpenter, B., Chamberlain, C. J., Cooper, A., Coutts, A., Cox, S. C., Craw, L., Eccles, J.

876 D., Faulkner, D., Grieve, J., Grochowski, J., Gulley, A., Hartog, A., Henry, G., Howarth, J.,

877 Jacobs, K., Kato, N., Keys, S., Kirilova, M., Kometani, Y., Langridge, R., Lin, W., Little, T.,

878 Lukacs, A., Mallyon, D., Mariani, E., Mathewson, L., Melosh, B., Menzies, C., Moore, J.,

879 Morales, L., Mori, H., Niemeijer, A., Nishikawa, O., Nitsch, O., Paris, J., Prior, D. J., Sauer,

880 K., Savage, M. K., Schleicher, A., Shigematsu, N., Taylor-Offord, S., Teagle, D., Tobin, H.,

881 Valdez, R., Weaver, K., Wiersberg, T. and Zimmer, M.: Petrophysical, Geochemical, and

882 Hydrological Evidence for Extensive Fracture-Mediated Fluid and Heat Transport in the

883 Alpine Fault's Hanging-Wall Damage Zone, Geochemistry, Geophys. Geosystems, 18(12),

884 4709–4732, doi:10.1002/2017GC007202, 2017.

885 Toy, V.: Rheology of the Alpine Fault mylonite zone: deformation processes at and below the

886 base of the seismogenic zone in a major plate boundary structure, University of Otago., 2008.

887 Toy, V. G., Prior, D. J. and Norris, R. J.: Quartz fabrics in the Alpine Fault mylonites:

888 Influence of pre-existing preferred orientations on fabric development during progressive

889 uplift, J. Struct. Geol., 30(5), 602–621, doi:10.1016/j.jsg.2008.01.001, 2008.

890 Toy, V. G., Craw, D., Cooper, A. F. and Norris, R. J.: Thermal regime in the central Alpine

891 Fault zone, New Zealand: Constraints from microstructures, biotite chemistry and fluid

892 inclusion data, Tectonophysics, 485(1–4), 178–192, doi:10.1016/j.tecto.2009.12.013, 2010.

893 Toy, V. G., Boulton, C. J., Sutherland, R., Townend, J., Norris, R. J., Little, T. A., Prior, D. J.,

894 Mariani, E., Faulkner, D., Menzies, C. D., Scott, H. and Carpenter, B. M.: Fault rock

895 lithologies and architecture of the central Alpine fault, New Zealand, revealed by DFDP-1

896 drilling, Lithosphere, 7(2), 155–173, doi:10.1130/l395.1, 2015.

897 Toy, V. G., Sutherland, R., Townend, J., Allen, M. J., Becroft, L., Boles, A., Boulton, C.,

898 Carpenter, B., Cooper, A., Cox, S. C., Daube, C., Faulkner, D. R., Halfpenny, A., Kato, N.,

899 Keys, S., Kirilova, M., Kometani, Y., Little, T., Mariani, E., Melosh, B., Menzies, C. D.,

900 Morales, L., Morgan, C., Mori, H., Niemeijer, A., Norris, R., Prior, D., Sauer, K., Schleicher,

901 A. M., Shigematsu, N., Teagle, D. A. H., Tobin, H., Valdez, R., Williams, J., Yeo, S., Baratin,

902 L. M., Barth, N., Benson, A., Boese, C., Célérier, B., Chamberlain, C. J., Conze, R.,

903 Coussens, J., Craw, L., Doan, M. L., Eccles, J., Grieve, J., Grochowski, J., Gulley, A.,

904 Howarth, J., Jacobs, K., Janku-Capova, L., Jeppson, T., Langridge, R., Mallyon, D., Marx, R.,

905 Massiot, C., Mathewson, L., Moore, J., Nishikawa, O., Pooley, B., Pyne, A., Savage, M. K.,

906 Schmitt, D., Taylor-Offord, S., Upton, P., Weaver, K. C., Wiersberg, T. and Zimmer, M.:

907 Bedrock geology of DFDP-2B, central Alpine Fault, New Zealand, New Zeal. J. Geol.

908 Geophys., 60(4), 497–518, doi:10.1080/00288306.2017.1375533, 2017.

909 Turnbull, I. M., Mortimer, N. and Craw, D.: Textural zones in the Haast Schist—a

910 reappraisal, New Zeal. J. Geol. Geophys., 44(1), 171–183,

911 doi:10.1080/00288306.2001.9514933, 2001.

912 Upton, P., Song, B. R. and Koons, P. O.: Topographic control on shallow fault structure and

913 strain partitioning near Whataroa, New Zealand demonstrates weak Alpine Fault, New Zeal.

914 J. Geol. Geophys., 1–8, doi:10.1080/00288306.2017.1397706, 2017.

915 Vermilye, J. M. and Scholz, C. H.: The process zone: A microstructural view of fault growth,

916 J. Geophys. Res. Earth, 103(B6), 12223–12237, doi:10.1029/98JB00957, 1998.

917 Warr, L. N. and Cox, S.: Clay mineral transformations and weakening mechanisms along the

918 Alpine Fault, New Zealand, in Geological Society, London, Special Publications, vol. 186,

919 edited by R. E. Holdsworth, R. A. Strachan, J. F. Magloughlin, and R. J. Knipe, pp. 85–101,

920   The Geological Society, London., 2001.

921   Wellman, H.: Data for the Study of Recent and Late Pleistocene Faulting in the South, New

922   Zeal. J. Sci. Technol., 34(4), 270–288, 1953.

923   Williams, J. N., Toy, V. G., Massiot, C., McNamara, D. D. and Wang, T.: Damaged beyond

924   repair? Characterising the damage zone of a fault late in its interseismic cycle, the Alpine

925   Fault, New Zealand, J. Struct. Geol., 90, 76–94, doi:10.1016/j.jsg.2016.07.006, 2016.

926   Williams, J. N., Toy, V. G., Smith, S. A. F. and Boulton, C.: Fracturing, fluid-rock interaction

927   and mineralisation during the seismic cycle along the Alpine Fault, J. Struct. Geol., 103, 151–

928   166, doi:https://doi.org/10.1016/j.jsg.2017.09.011, 2017a.

929   Williams, J. N., Toy, V. G., Massiot, C. and McNamara, D.: X-ray Computed Tomography

930   and borehole televiewer images of the Alpine Fault's hanging-wall, New Zealand: Deep Fault

931   Drilling Project phase 1 (DFDP-1) and Amethyst Hydro Project (AHP), GFZ Data Serv.,

932   doi:http://doi.org/10.5880/ICDP.5052.004, 2017b.

933   Wilson, J. E., Chester, J. S. and Chester, F. M.: Microfracture analysis of fault growth and

934   wear processes, Punchbowl Fault, San Andreas system, California, J. Struct. Geol., 25(11),

935   1855–1873, doi:10.1016/S0191-8141(03)00036-1, 2003.

936   Wright, C. A.: Geology and paleoseismicity of the central Alpine Fault, New Zealand., 1998.

937   Yukutake, Y., Ito, H., Honda, R., Harada, M., Tanada, T. and Yoshida, A.: Fluid-induced

938   swarm earthquake sequence revealed by precisely determined hypocenters and focal

939   mechanisms in the 2009 activity at Hakone volcano, Japan, J. Geophys. Res. Solid Earth,

940   116(4), doi:10.1029/2010JB008036, 2011.

941   Zangerl, C., Loew, S. and Eberhardt, E.: Structure, geometry and formation of brittle

942   discontinuities in anisotropic crystalline rocks of the central Gotthard massif, Switzerland,

943   Eclogae Geol. Helv., 99(2), 271–290, doi:10.1007/s00015-006-1190-0, 2006.

944

946 **Figure 1**
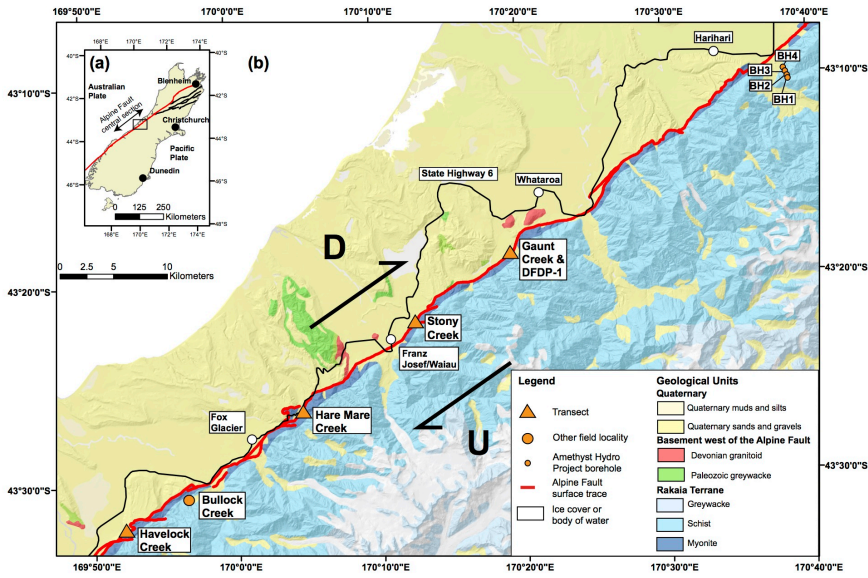
947

948 Figure 1: (a) Location map for Alpine Fault (red line) and Marlborough Faults (black line) in the

949 South Island of New Zealand. Box shows extent of (b), a location map for the DFDP-1 and AHP

950 boreholes, and field transects. The generalised underlying geology is derived from the GNS Science

951 1:250000 QMAP project (Rattenbury and Isaac, 2012) and has been draped over a digital elevation

952 model (Columbus et al., 2011).

953

954 **Figure 2**
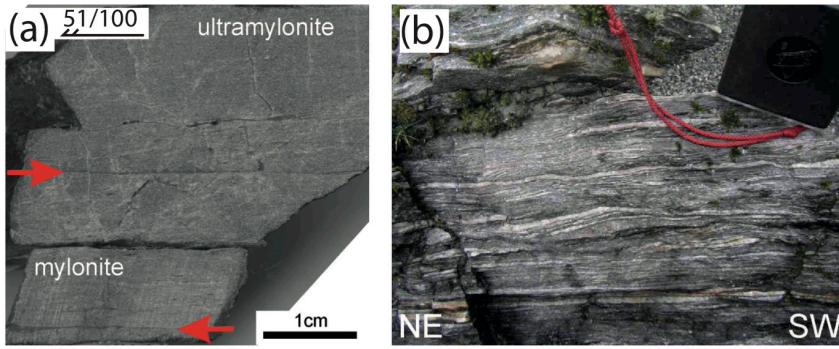
955

956 Figure 2: (a) Quartzofeldspathic Alpine Fault ultramylonite that gradually grades to mylonite at the

957 base of the image from Gaunt Creek (43°19'00.62" S, 170°19'32.79" E). A foliation defined by

958 alternating white quartzofeldspathic bands and dark grey mica bands is hard to distinguish in the

959 ultramylonite but is more apparent in the mylonite. (b) The well foliated Alpine Fault protomylonite-

960 mylonite transition at Gaunt Creek (43°19'05.11" S, 170°19'46.16" E). Compass is 5 cm wide. Both

961 images previously presented in Toy, (2008).

962

Deleted: The sample in (a) was taken from Gaunt Creek, as was the photo in (b).

965 **Figure 3**
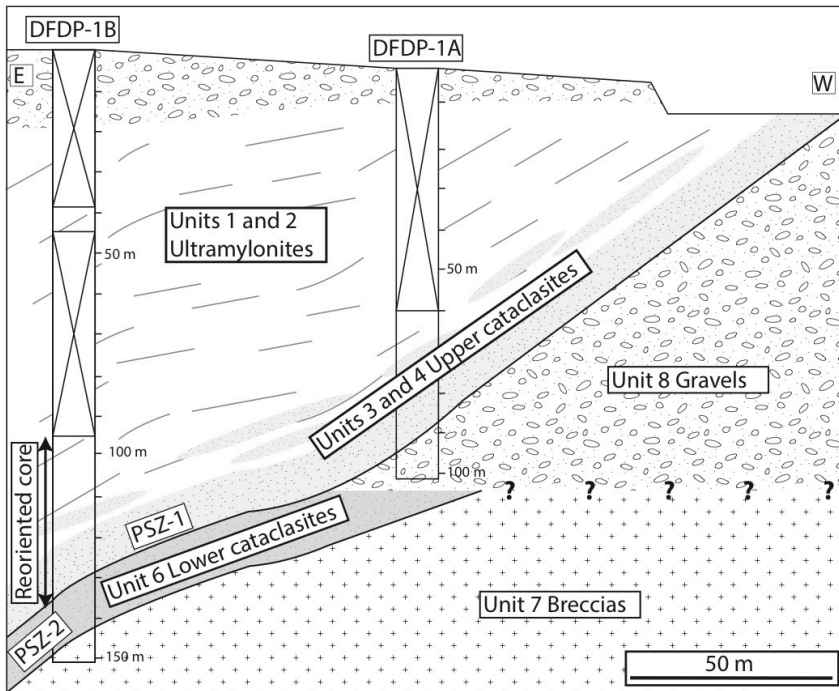
966

967 Figure 3: Cross section through the DFDP-1 boreholes, showing interval where reoriented drill-core is

968 located. Boxes with diagonal lines depict intervals in borehole with no core recovery, grey lines

969 represent mylonitic foliation. Modified from Sutherland et al., (2012), with lithological units

970 previously defined by Toy et al., (2015).

971
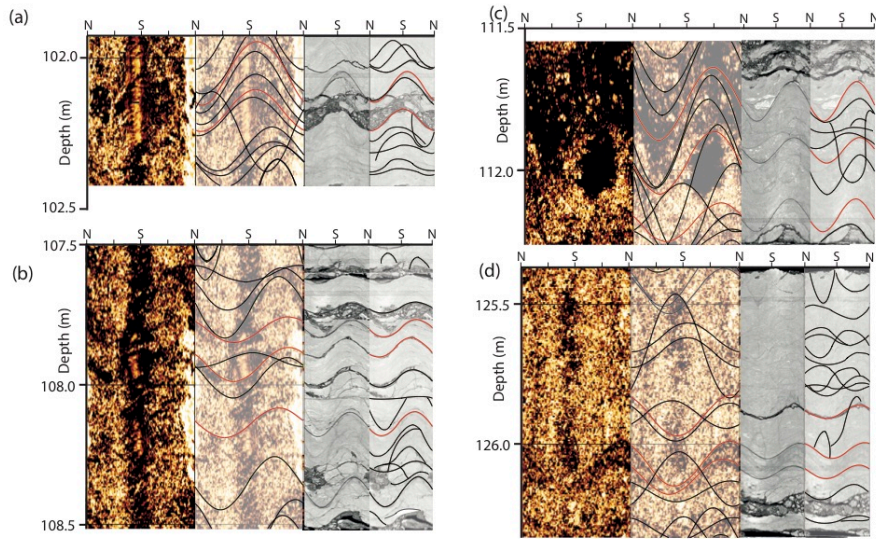
 Figure 4

973

974 Figure 4: Examples of matching structures between BHTV images and unrolled CT images. In each

975 image, the first two columns are the BHTV amplitude image, without and with interpretations

976 respectively, whilst the third and fourth columns depict the unrolled CT image over the same interval,

977 also without and with interpretations. Fractures that have been traced in red indicate those that were

978 matched to reorientate core.

979
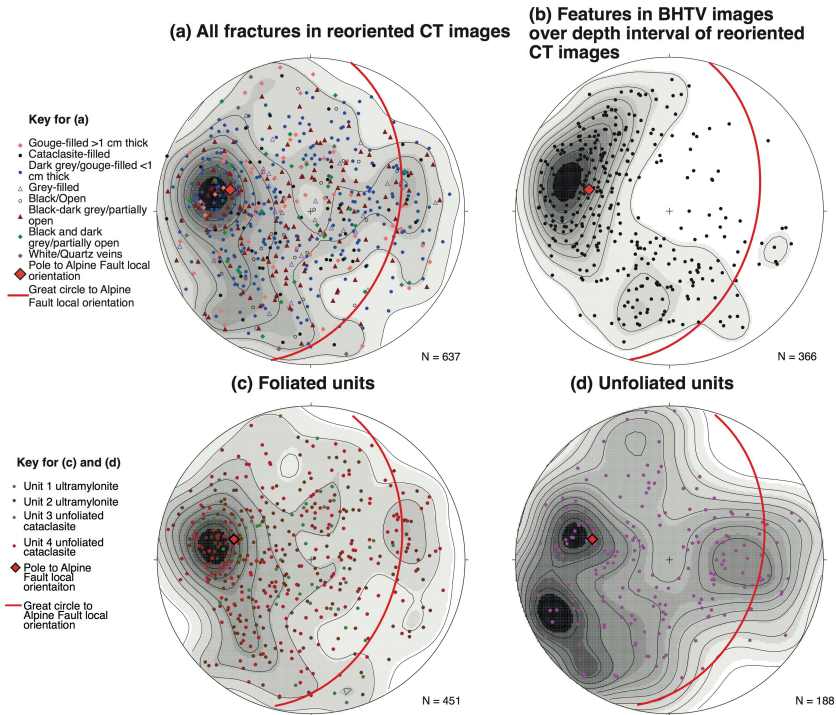
 Figure 5

Figure 5: Lower hemisphere equal area stereoplots depicting orientation of fractures in DFDP-1.

Contouring on stereoplots was applied to poles that are weighted depending on their orientation

correction *w* (see Sect. 3.2), and that are rounded to the nearest whole number. Contours were then

generated for the weighted poles using a probability distribution calculated by a Kernel function in the

RFOC package for R (Lees, 2014). Great circle represents orientation of Alpine Fault plane and

foliation at DFDP-1 site (Townend et al., 2013). (a) Orientation of all fractures that were reoriented by

matching structures between unrolled CT images and BHTV images, sorted by fracture type (Williams

et al., 2016). (b) Orientation of features recognised in the BHTV images over the interval of reoriented

core (94-126 m in DFDP-1B). Fracture orientations extracted from reoriented DFDP-1 CT images in

(c) foliated units and (d) unfoliated units, using the DFDP-1 lithological classification scheme (Toy et

al., 2015).

993 **Figure 6**

CT Number Key: 500 2250 4000
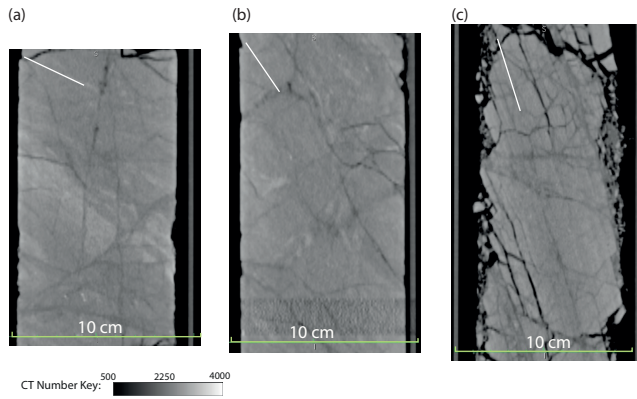
994

995 Figure 6: The relationship between foliation and fracture orientations in Alpine Fault ultramylonite, as

996 observed in 2D CT image slices of DFDP-1 drill-core. Intervals are (borehole, core section and run,

997 depth interval): (a) DFDP-1A 55-1 75.45-75.62 m, (b) DFDP-1B 35-1 102.49-102.64 m, and (c)

998 DFDP-1B 25-2, 44.80-45.20 m. In (a) and (b) fractures tend to cross-cut the ultramylonitic foliation

999 (orientation represented by white line in top left corner of each image). (c) Fractures show a greater

1000 preference to be aligned parallel to the foliation. Note that (c) was previously shown in Williams et al.,

1001 (2016), and is not included in the reorientation analysis in Figure 5, as there was no BHTV imagery

1002 for this interval.

1004   **Figure 7**
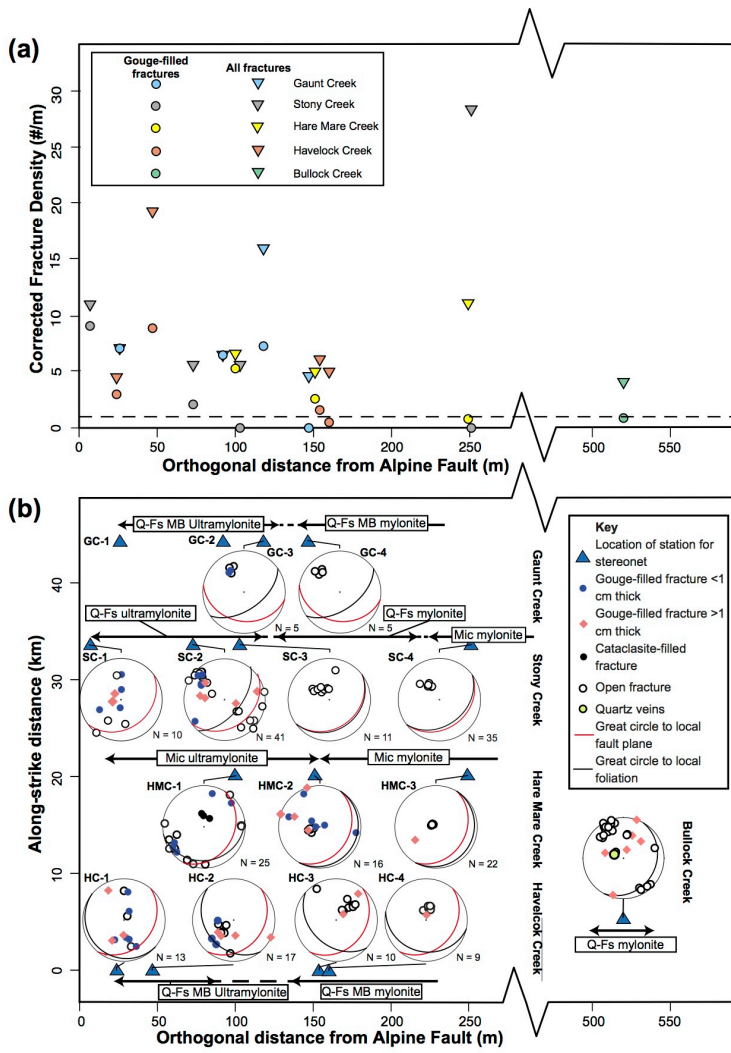
1005

1006   Figure 7: (a) Corrected fracture density at all stations for gouge-filled fractures and all fractures.

1007   Dashed line indicates a corrected fracture density of 1 fracture/metre. No orientation data was

1008   collected at Gaunt Creek stations 1 and 2, so fracture density is calculated from the two perpendicular

1009   transects. (b) Compilation of stereoplots for fracture orientations at each field station. Stations have

1010 been plotted as a function of distance from the fault and distance along-strike (with respect to

1011 Havelock Creek) along within fault rock lithologies (Toy, 2008). Dashed lines indicate gradational or

1012 obscured lithological boundaries. Qfs, Quartzofeldspath; MB, metabasic; Mic, Micaceous. For field

1013 cross sections and location of stations, see Figure S1 and Table S2.

1016 **Figure 8**
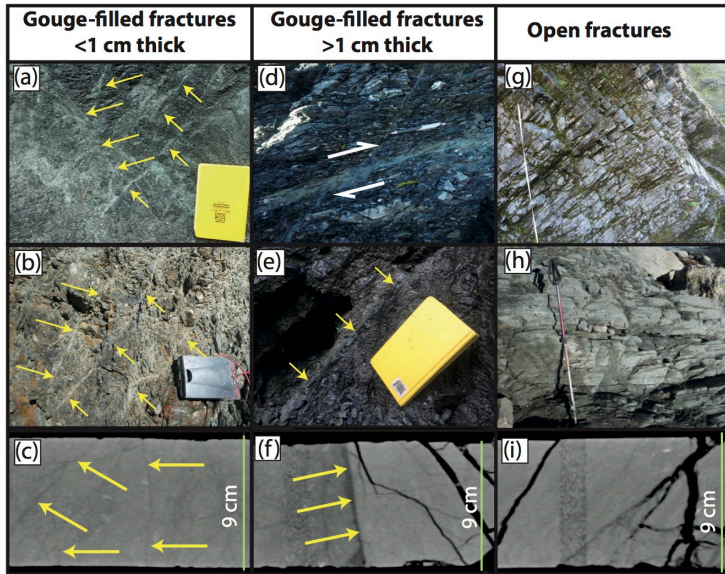
1017

1018 Figure 8: Examples of the three main types of fractures observed in the field around the Alpine Fault,

1019 and correlative fractures in DFDP-1 CT scans. (a-c) Thin gouge-filled fractures (yellow arrows) have a

1020 range of orientations and found exclusively within 160 m from the fault. They are equivalent to type

1021 iii of fractures from Williams et al., (2016). (d-f) Thicker gouge and cataclasite filled fractures are

1022 equivalent to type i and ii fractures of Williams et al. (2016) and may be observed at all distances from

1023 the Alpine Fault. Offset markers can be observed across these fractures (e.g. the vein indicated by the

1024 pen and white arrows in (d)). (g-i) Open fractures are mainly foliation-parallel. Equivalent to type v

1025 fractures of Williams et al., (2016). Location of field photos: (a) Waikukupa thrust (43°26' 34.7" S,

1026 170°04'10.9" E), (b) Stony Creek 2, (d) Havelock Creek 2, (e) Bullock Creek, (g) Stony Creek

1027 (43°22'23.92" S, 170°12'53.63" E), (h), Havelock Creek 4. Compass clinometer 8 cm and yellow

1028 notebook 20 cm in length. Measuring tape in (e) 1.1 m long, walking pole in (g) 1 m in length. DFDP-

1029 1 CT scan intervals: (c) DFDP-1B 56-2 125.35-125.49 m, (f) DFDP-1B 35-1 102.00-102.15 m, (i)

1030 DFDP-1B 33-2 99.45-99.60 m
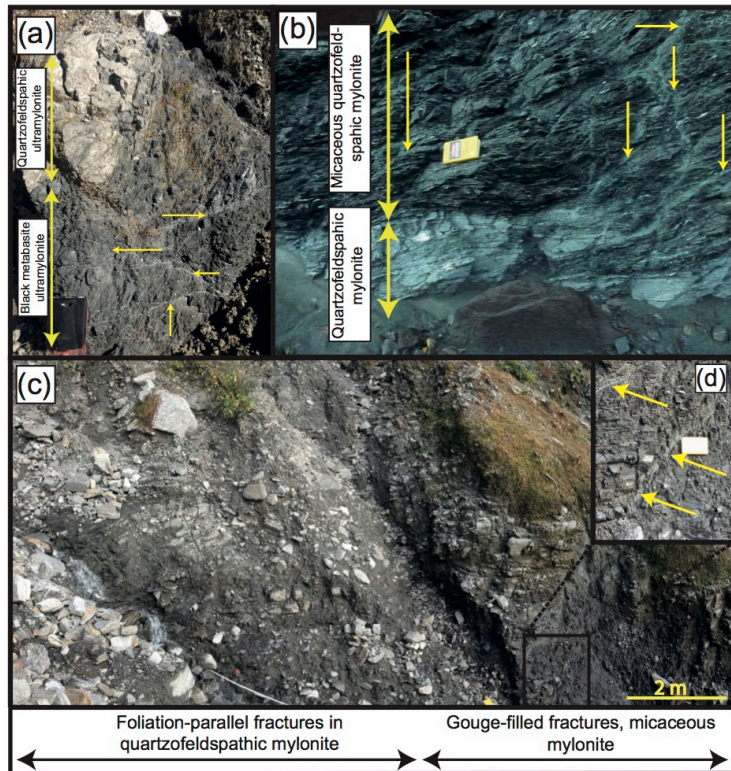
1034

Figure 9: Field observations of changes in fracture density at lithological contacts. (a&b) Intervals of

micaceous and metabasite mylonite containing a relatively high proportion of gouge filled fractures

(denoted by yellow arrows) compared to interlayered quartzofeldspathic mylonite. (c) Transition from

micaceous mylonite to quartzofeldspathic mylonite coincides with furthest extent of intensive gouge-

filled fractures, as shown by yellow arrows in (d). Taken at (a) Gaunt Creek 1, (b) Havelock Creek 2,

(c&d) Hare Mare Creek 3. Compass clinometer 8 cm and yellow notebook 20 cm in length.

1041 **Figure 10**
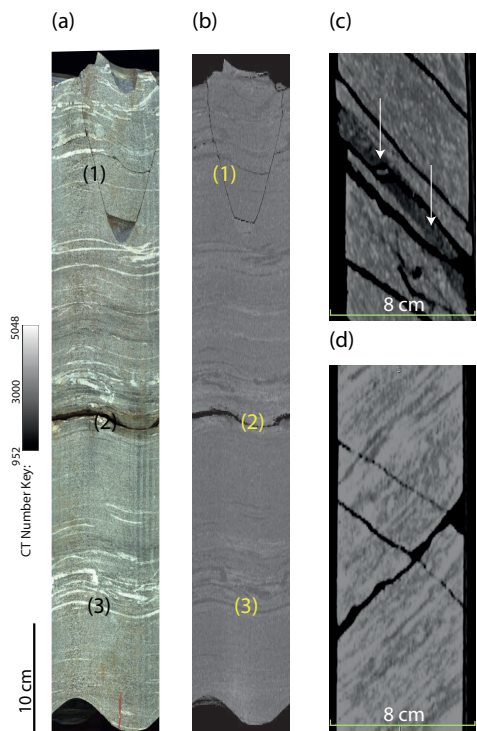
1042

1043 Figure 10: Fractures in the Amethyst Hydro Project (AHP) drill-core. Unrolled images of AHP drill-

1044 core (BH1 45-2 124.3-124.9 m) taken by (a) DMT core scanner and (b) generated from a CT image.

1045 (1) Identifies fracture cutting across foliation, (2) foliation-parallel fracture with alteration halo, (3)

1046 foliation defined by quartzofeldspathic bands that have low CT numbers. (c&d) Core-axial parallel CT

1047 image slices of AHP drill-core. In (c) white arrows point to a 'crush zone' sub parallel to foliation

1048 (BH2 75-2 155.92-156.04 m). (d) more variable fracture orientations identified in BH4 (Section 70-4

1049 196.62-196.80 m).

1050

1051 **Figure 11**
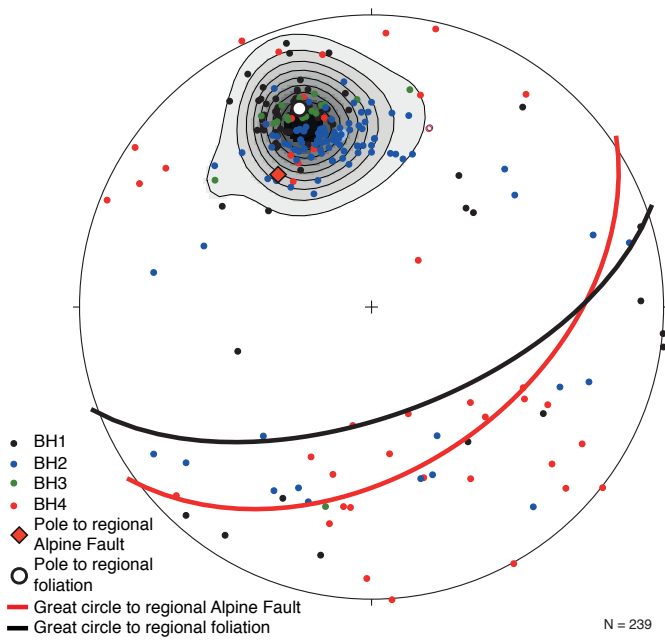
1052

1053 Figure 11: Equal area, lower hemisphere projection of fracture orientations recognised in CT scans of

1054 AHP drill-core separated by borehole. Contours plotted with weighted poles (see Figure 5).

1055

1056   **Figure 12**
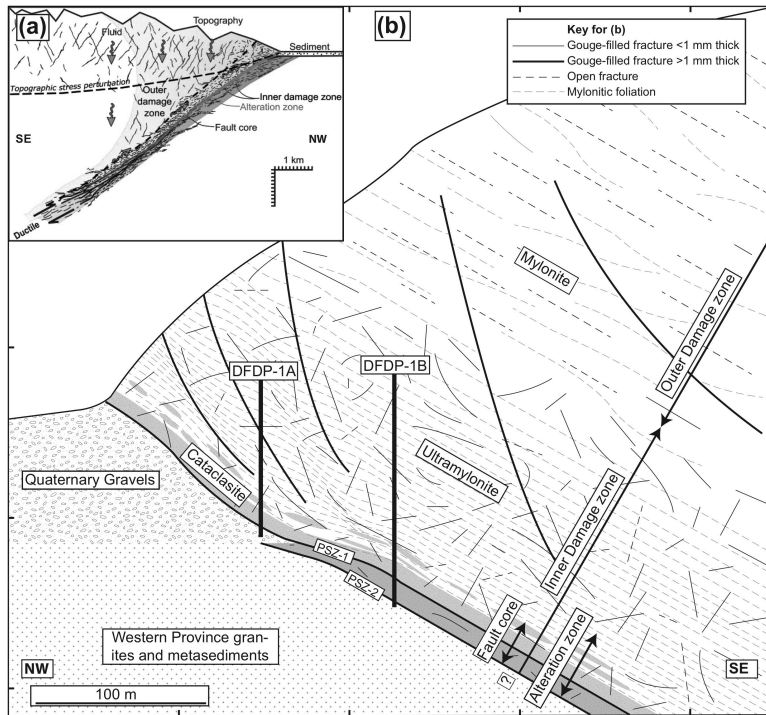
1057

1058   Figure 12: Schematic cross sections through the Alpine Fault illustrating its hanging-wall

1059   structure. (a) Crustal-scale cross section illustrating the flower shaped geometry of the outer

1060   damage zone (after Townend et al., (2017)). (b) A thrust section within the central section of

1061   the Alpine Fault, depicting fracture network, its relationship to foliation, and the distribution

1062   of subsidiary faults. Respective position of DFDP-1 boreholes also shown. Constructed from

1063   cross sections previously presented in Norris and Cooper, (2007) and Sutherland et al.,

1064   (2012).

1065   **Figure 13**
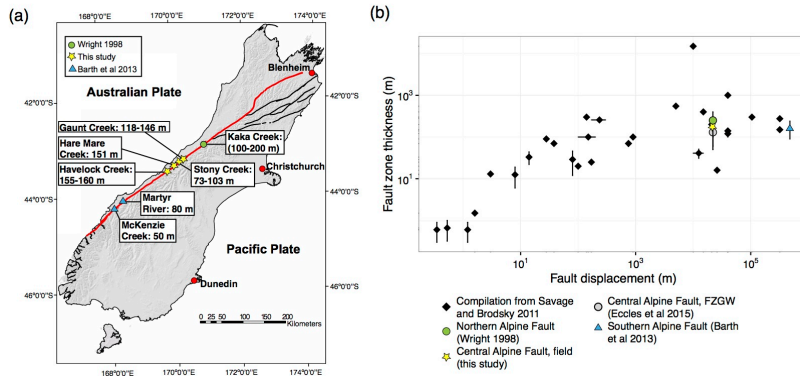
1066

1067   Figure 13: (a) Compilation of estimates of the 'inner damage zone' width on the Pacific Plate

1068   side of the Alpine Fault (red line) from four creek sections in this study (Gaunt Creek, Stony

1069   Creek, Hare Mare Creek and Havelock Creek). This is combined with other along-strike

1070   estimates of damage zone thickness for the Pacific Plate side of the Alpine Fault: McKenzie

1071   Creek and Martyr River (Barth et al., 2013) and Kaka Creek (Wright, 1998). (b) Log-log plot

1072   of fault zone thickness as a function of fault displacement previously presented in Savage and

1073   Brodsky, (2011), combined with estimates made for the Alpine Fault assuming footwall

1074   damage is no more extensive than in the hanging-wall. Displacement for the Alpine Fault is

1075   480 km (Norris and Cooper, 2007; Wellman, 1953). However, convergence along the Alpine

1076   Fault's central section requires that it erodes its own fault rocks so these points are plotted to

1077   reflect only the brittle displacement the rocks themselves have accommodated as they are

1078   exhumed through the seismogenic zone (22 km, Barth et al., (2012)). Error bars reflect

1079   uncertainty in constraining fault zone width (as for example, footwall damage is largely

1080   unknown), not necessarily variability in fault zone thickness.

1081

1082   **Figure A1**
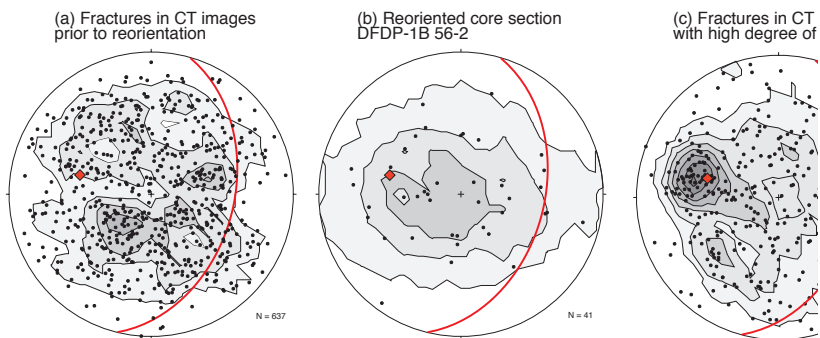
1083

1084   Figure A1: Stereoplots to tests the confidence in reorientations applied to rotate DFDP-1 CT

1085   scan fracture orientations into geographic coordinates. Red great circle and diamond in each

1086   plot represents plane and pole to the Alpine Fault orientation measured in DFDP-1B. Plotted

1087   with Kamb contours with intervals of two standard deviations. (a) Orientation of fractures

1088   shown in Figure 5a before rotation, (b) orientation of reoriented fractures within a single core

1089   section (DFDP-1B 56-2), and (c) orientation of fractures in CT images from core sections that

1090   were oriented with a high degree of confidence with BHTV images.

1091

1093 **Table 1**

	Number of fractures	Resultant Plane dip direction	Resultant Plane dip	Resultant vector length (Cluster intensity, 2 s.f.)
All reoriented DFDP-1 CT fractures	637	80	58	0.58
Reoriented DFDP-1 CT fractures, foliated units	451	87	58	0.58
Reoriented DFDP-1 CT fractures, unfoliated units	188	71	61	0.58
DFDP-1B BHTV features (depth interval 94-126 m)	365	103	47	0.72
AHP Fractures	239	164	58	0.76

1094 Table 1: Clustering analysis of the different fracture datasets documented in this study, using

1095 the resultant vector methodology outlined by Priest, (1993). DFDP-1 foliated units comprise

1096 ultramylonites and foliated cataclasites (Units 1, 2 and 4 of Toy et al., (2015)). DFDP-1

1097 unfoliated units comprise unfoliated cataclasites (Unit 3 of Toy et al., (2015)). The resultant

1098 vector orientation for each dataset, which has been converted to spherical coordinates, is also

1099 reported. See text for full details.